



**HAL**  
open science

# Pluto's Beating Heart Regulates the Atmospheric Circulation: Results From High-Resolution and Multiyear Numerical Climate Simulations

T. Bertrand, F. Forget, O. White, B Schmitt, S. Stern, H. Weaver, L. Young,  
K. Ennico, C. Olkin

► **To cite this version:**

T. Bertrand, F. Forget, O. White, B Schmitt, S. Stern, et al.. Pluto's Beating Heart Regulates the Atmospheric Circulation: Results From High-Resolution and Multiyear Numerical Climate Simulations. *Journal of Geophysical Research. Planets*, 2020, 125 (2), pp.e2019JE006120. 10.1029/2019JE006120 . hal-03097621

**HAL Id: hal-03097621**

**<https://hal.science/hal-03097621v1>**

Submitted on 5 Jan 2021

**HAL** is a multi-disciplinary open access archive for the deposit and dissemination of scientific research documents, whether they are published or not. The documents may come from teaching and research institutions in France or abroad, or from public or private research centers.

L'archive ouverte pluridisciplinaire **HAL**, est destinée au dépôt et à la diffusion de documents scientifiques de niveau recherche, publiés ou non, émanant des établissements d'enseignement et de recherche français ou étrangers, des laboratoires publics ou privés.

**1 Pluto's beating heart regulates the atmospheric**  
**2 circulation: results from high resolution and**  
**3 multi-year numerical climate simulations**

T. Bertrand<sup>1</sup>, F. Forget<sup>2</sup>, O. White<sup>1</sup>, B. Schmitt<sup>3</sup>, S. A. Stern<sup>4</sup>, H. A.

Weaver<sup>5</sup>, L. A. Young<sup>4</sup>, K. Ennico<sup>1</sup>, C.B. Olkin<sup>4</sup>, and the New Horizons

Science Team

---

Corresponding author: T. Bertrand, National Aeronautics and Space Administration (NASA), Ames Research Center, Space Science Division, Moffett Field, CA 94035, USA (tanguy.bertrand@nasa.gov)

<sup>1</sup>National Aeronautics and Space

**Key Points.**

- High-resolution simulations of Pluto's climate show that the circulation is dominated by  $\sim 10 \text{ m s}^{-1}$  retrograde winds during most of the year
- Nitrogen condensation-sublimation flows in Sputnik Planitia are creating an intense western boundary current.
- Atmospheric heat flux, transport of tholins and albedo feedbacks could explain the albedo contrasts observed in Sputnik Planitia.

---

Administration (NASA), Ames Research  
Center, Space Science Division, Moffett  
Field, CA 94035, United States

<sup>2</sup>Laboratoire de Météorologie Dynamique,  
IPSL, Sorbonne Universités, UPMC Univ  
Paris 06, CNRS, 4 place Jussieu, 75005  
Paris, France

<sup>3</sup>Université Grenoble Alpes, CNRS,  
Institut de Planétologie et Astrophysique de  
Grenoble, Grenoble F-38000, France

<sup>4</sup>Southwest Research Institute, Boulder,  
CO 80302, United States

<sup>5</sup>Johns Hopkins University Applied  
Physics Laboratory, Laurel, MD, 20723,  
United States

4 **Abstract.** Pluto’s atmosphere is mainly nitrogen and is in solid-gas equi-  
5 librium with the surface nitrogen ice. As a result, the global nitrogen ice dis-  
6 tribution and the induced nitrogen condensation-sublimation flows strongly  
7 control the atmospheric circulation. It is therefore essential for Global Cli-  
8 mate Models (GCMs) to accurately account for the global nitrogen ice dis-  
9 tribution in order to realistically simulate Pluto’s atmosphere. Here we present  
10 a set of new numerical simulations of Pluto’s atmosphere in 2015 performed  
11 with a GCM using a 50-km horizontal resolution ( $3.75^\circ \times 2.5^\circ$ ) and taking  
12 into account the latest topography and ice distribution data, as observed by  
13 the New Horizons spacecraft. In order to analyze the seasonal evolution of  
14 Pluto’s atmosphere dynamics, we also performed simulations at coarser res-  
15 olution ( $11.25^\circ \times 7.5^\circ$ ) but covering three Pluto years. The model predicts  
16 a near-surface western boundary current inside the Sputnik Planitia basin  
17 in 2015, which is consistent with the dark wind streaks observed in this re-  
18 gion. We find that this atmospheric current could explain the differences in  
19 ice composition and color observed in the north-western regions of Sputnik  
20 Planitia, by significantly impacting the nitrogen ice sublimation rate in these  
21 regions through processes possibly involving conductive heat flux from the  
22 atmosphere, transport of dark materials by the winds and surface albedo pos-  
23 itive feedbacks. In addition, we find that this current controls Pluto’s gen-  
24 eral atmospheric circulation, which is dominated by a retro-rotation, inde-  
25 pendently of the nitrogen ice distribution outside Sputnik Planitia. This ex-

26    otic circulation regime could explain many of the geological features and lon-  
27    gitudinal asymmetries in ice distribution observed all over Pluto's surface.

## 1. Introduction

28 Among the most striking observations of Pluto, made by the cameras aboard New  
29 Horizons during the July 2015 flyby, is a planetary-scale multi-km-thick equatorial N<sub>2</sub>-  
30 rich ice sheet (mixed with small amounts of CO and CH<sub>4</sub>), covering the floor of the  
31 Sputnik Planitia basin that extends between latitudes 25°S-50°N at a level 3 km below  
32 the surrounding terrains [Stern et al., 2015; Grundy et al., 2016; Schenk et al., 2018].  
33 Highlands to the east of this structure are also covered by N<sub>2</sub>-rich ices, which merge  
34 with the ices of Sputnik Planitia through several valley glaciers [Protopapa et al., 2017;  
35 Schmitt et al., 2017; Howard et al., 2017]. Both regions form the left and right lobe  
36 of the heart-shaped Tombaugh Regio, likely the most active geological region on Pluto.  
37 Other observed reservoirs of N<sub>2</sub>-rich ice include northern mid-latitudinal deposits mainly  
38 concentrated in local depressions, while CH<sub>4</sub>-rich ice has been detected around the north  
39 pole and at the equator where it forms the massive “Bladed Terrain” deposits [Moores  
40 et al., 2017; Moore et al., 2018] and at the northern fringe of Cthulhu Macula.

41 Volatile transport models have been able to simulate the cycle of N<sub>2</sub> and CH<sub>4</sub> over  
42 different timescales and understand to first order the observed distribution of these ices  
43 across Pluto’s surface [Hansen and Paige, 1996; Young, 2013; Toigo et al., 2015; Bertrand  
44 and Forget, 2016]. In particular, it has been shown that N<sub>2</sub> ice tends to accumulate in  
45 Sputnik Planitia due to its low elevation corresponding to a higher pressure and conden-  
46 sation temperature [Bertrand and Forget, 2016]. Outside the basin, observed latitudinal  
47 bands of N<sub>2</sub> and CH<sub>4</sub> deposits were reproduced by models (to first order) and shown to be  
48 related to the seasonal and astronomical cycles [Protopapa et al., 2017; Bertrand et al.,

2018, 2019]. However, some of the observed longitudinal asymmetries in ice distribution,  
composition, texture or color could not be explained by these models. For instance, the  
equatorial regions west of Sputnik Planitia are volatile-free and covered by a dark mantle  
of organic materials (tholins), while the regions east of Sputnik Planitia are covered by  
N<sub>2</sub>-rich and CH<sub>4</sub>-rich ices, including the Bladed Terrain deposits which extend between  
210°E and 40°E [Moore et al., 2018]. If the accumulation of CH<sub>4</sub> ice is predicted in the  
equatorial regions [Bertrand et al., 2019], this asymmetry in longitude remains a mystery.  
Another example is Sputnik Planitia’s ice sheet itself, which displays bright and dark N<sub>2</sub>  
ice plains, the latter being enriched in dark red material and in CH<sub>4</sub> ice and located in the  
northern and western regions of Sputnik Planitia (see Fig. 35 and 36 in Schmitt et al.  
[2017] and Fig. 5 in Protopapa et al. [2017]).

Runaway albedo and volatile variations as well as differential condensation and sublima-  
tion have been suggested to explain these features [White et al., 2017; Moore et al., 2018;  
Earle et al., 2018], but the role of atmospheric circulation may be crucial and remains to  
be explored. Besides, the observations of wind streaks and eolian linear dunes on Pluto’s  
surface [Stern et al., 2015; Telfer et al., 2018] are indications that Pluto’s atmospheric  
dynamics can impact the surface geology.

Previous GCM modeling studies investigated the dynamics of the 1-Pa atmosphere of  
Pluto in 2015 and showed how near-surface winds (below 1000 m altitude) and the general  
circulation are controlled by the topography and the N<sub>2</sub> condensation-sublimation flow  
[Toigo et al., 2015; Forget et al., 2017]. In particular, Forget et al. [2017] used a post-New  
Horizons version of the Pluto GCM developed at the Laboratoire de Météorologie Dy-  
namique (LMD), and performed a comprehensive characterization of the dynamics within

72 Pluto's atmosphere (wind regimes, waves, cloud formation, temperatures etc.). They  
73 showed that down-slope katabatic winds dominate everywhere across Pluto, as a result of  
74 surface temperatures being much colder than those in the atmosphere. At locations close  
75 to N<sub>2</sub> ice deposits, katabatic winds may be balanced during daytime by N<sub>2</sub> sublimation  
76 flows, and strengthened during nighttime by condensation flows.

77 Forget et al. [2017] highlighted the sensitivity of the general circulation to the atmo-  
78 spheric transport of N<sub>2</sub> and therefore to the locations of the sources and sinks of N<sub>2</sub> on the  
79 surface. They obtained three different dynamical circulation regimes for 2015, depending  
80 on the initial location of the N<sub>2</sub> ice deposits: (1) If N<sub>2</sub> ice was placed in Sputnik Plani-  
81 tia and on the poles, they predicted a retro-rotation, induced by conservation of angular  
82 momentum as N<sub>2</sub> is transported from one hemisphere to another, as also found by Toigo  
83 et al. [2015]. (2) If N<sub>2</sub> ice was placed in Sputnik Planitia and at the south pole, then the  
84 model predicted an intense condensation flux at the south pole leading to the formation of  
85 a prograde jet at high altitude, and, through mechanisms of wave instabilities, to a zonal  
86 circulation characterized by a super-rotation, like on Venus and Titan. (3) Lastly, if N<sub>2</sub>  
87 ice was placed in Sputnik Planitia only, the zonal winds obtained were weak and induced  
88 by a thermal gradient between both hemispheres. However, in this first low-resolution  
89 version of the LMD Pluto GCM, the Sputnik Planitia basin was represented as a simple  
90 circular crater located north of the equator. In reality, the Sputnik Planitia basin and  
91 ice sheet extend southward down to 25°S. This should trigger significant cross-equatorial  
92 transport of N<sub>2</sub> and impact the general atmospheric circulation.

93 Here we run higher resolution simulations of Pluto's atmosphere using the latest ver-  
94 sion of the LMD Pluto GCM coupled with New Horizons topography data. Our primary

95 purpose is to describe the general circulation of Pluto’s atmosphere in 2015, detail the  
96 near-surface circulation within Sputnik Planitia and provide explanation for some obser-  
97 vations made by New Horizons, which will complement the work of Forget et al. [2017].  
98 Section 2 presents the models and the methods used to reach consistent equilibrated at-  
99 mosphere and surface conditions in the GCM. It also includes a description of the set of  
100 simulations used in this paper, which differ by their initial surface N<sub>2</sub> ice distribution. We  
101 present the model results in two different sections. Section 3 describes the near-surface  
102 circulation in Sputnik Planitia and compares the results with the available observations,  
103 whereas Section 4 describes the general circulation obtained for 2015. We also present  
104 preliminary results of a GCM simulation extending over three Pluto years. We discuss  
105 further these results and their implications on Pluto’s climate in Section 5.

## 2. Model description

106 Our analysis was performed using the LMD three-dimensional GCM of Pluto [Forget  
107 et al., 2017; Bertrand and Forget, 2017] which includes atmospheric dynamics and trans-  
108 port, turbulence, radiative transfer, molecular conduction as well as phases changes for  
109 N<sub>2</sub>, CH<sub>4</sub> and CO.

### 2.1. Recent improvements of the GCM

110 The model has recently been improved and now takes into account: (1) A digital eleva-  
111 tion model (DEM) of the encounter hemisphere derived from New Horizons stereo imaging  
112 [Schenk et al., 2018]. We use flat topography for most of the non-observed hemisphere (see  
113 Section 2.3) as well as for the southern non-illuminated polar region (note that this has  
114 no impact on the results of this paper). (2) The presence of perennial CH<sub>4</sub>-rich deposits

115 in the equatorial regions (Bladed Terrains). On Pluto, these terrains are characterized  
116 by a high elevation (above 2 km), parallel sets of “blades“ (steep ridges and sharp crests)  
117 and a relatively dark albedo [0.5-0.6 Buratti et al., 2017]. They are visible in the Tartarus  
118 Dorsa region (east of Sputnik Planitia) but their distinctive CH<sub>4</sub> absorption is seen in  
119 low resolution coverage of Pluto obtained during the New Horizons approach phase, sug-  
120 gesting that Bladed Terrain may occur in patches further east along the equator [Olkin  
121 et al., 2017; Moore et al., 2018]. In the model, we place a CH<sub>4</sub> ice reservoir at the loca-  
122 tions of these terrains (inexhaustible over the timescales considered in this paper) with a  
123 topography similar to that of the resolved Bladed Terrains in Tartarus Dorsa. (3) A dual  
124 surface albedo for CH<sub>4</sub> ice: we use a CH<sub>4</sub> ice albedo of 0.5 for the equatorial deposits and  
125 an albedo between 0.65-0.75 for the polar CH<sub>4</sub> deposits (see Section 2.3), based on albedo  
126 maps of Pluto [Buratti et al., 2017].

## 2.2. General setting, initial and boundary conditions

127 Because Pluto orbits far from the Sun, its seasonal cycle is much longer than on Earth  
128 (one Pluto year is  $\sim 248$  Earth years). Above all, Pluto receives very little energy, which  
129 results in low sublimation-condensation rates and slow surface processes. This is an issue  
130 for Pluto GCMs because the simulations need to be performed over many Pluto years  
131 in order to be insensitive to the initial state. To solve this issue and obtain a physically  
132 self-consistent, equilibrated combination of initial surface conditions for the GCM (soil  
133 temperatures, ice distributions), we use the 2D LMD volatile transport model (VTM) of  
134 Pluto [Bertrand and Forget, 2016], and create an initial state for the GCM which is the  
135 result of 30 million years of volatile ice evolution, with N<sub>2</sub> ice filling and flowing inside

136 Sputnik Planitia [Bertrand et al., 2018, 2019]. A similar method has been used by Forget  
137 et al. [2017] and Toigo et al. [2015].

138     The radiative constant for Pluto’s atmosphere, i.e. the time needed by the atmosphere  
139 to respond to a radiative forcing, is typically 10-15 Earth years [Strobel et al., 1996; Forget  
140 et al., 2017]. Therefore we start our 3D GCM simulations in 1984, so that the atmosphere  
141 reaches a realistic regime in 2015, insensitive to the initial state. The long-term VTM  
142 simulations and the low resolution GCM simulations are carried out with a horizontal  
143 grid of  $32 \times 24$  points to cover the globe (i.e.  $11.25^\circ \times 7.5^\circ$ ,  $\sim 150$  km in latitude) and 27  
144 vertical levels (the altitude of the first mid-layers are 5 m, 12 m, 25 m, 40 m, 80 m and  
145 the model top is at 250 km). The years 2014 and 2015 are then simulated at a higher  
146 spatial resolution by using a grid of  $96 \times 72$  points ( $3.75^\circ \times 2.5^\circ$ ,  $\sim 50$  km in latitude) and  
147 47 vertical levels (we use a finer vertical grid in the first 10 km, and the model top remains  
148 at 250 km).

149     The GCM simulations have been performed using an  $N_2$  ice emissivity of 0.8 and an  
150 albedo between 0.67-0.74 (see Section 2.3). The surface  $N_2$  pressure simulated in the  
151 model is constrained by these values and reaches 1-1.2 Pa in 2015 as observed by New  
152 Horizons. The albedo and emissivity of the bare ground (volatile-free surface) are set  
153 to 0.1 and 1 respectively, which corresponds to a terrain covered by dark red materials  
154 such as the informally named Cthulhu Macula.  $CH_4$  ice emissivity is fixed at 0.8 in all  
155 simulations. The thermal conduction into the subsurface is performed with a low thermal  
156 inertia near the surface set to  $20 \text{ J s}^{-1/2} \text{ m}^{-2} \text{ K}^{-1}$  to capture the short-period diurnal  
157 thermal waves and a larger thermal inertia below set to  $800 \text{ J s}^{-1/2} \text{ m}^{-2} \text{ K}^{-1}$  to capture  
158 the much longer seasonal thermal waves that can penetrate deep into the high thermal

159 inertia substrate. The rest of the settings are similar to those in Forget et al. [2017] and  
 160 Bertrand and Forget [2017].

### 2.3. The set of simulations: 3 scenarios explored

161 The GCM simulations presented in this paper are derived from our most realistic VTM  
 162 simulations, which best reproduce the threefold increase of surface pressure between 1988  
 163 and 2015 [Meza et al., 2019], with 1-1.2 Pa in 2015 [Stern et al., 2015]. We found three  
 164 possible scenarios for the N<sub>2</sub> surface ice distribution:

- 165 • Scenario #1: No N<sub>2</sub> ice deposits outside Sputnik Planitia.
- 166 • Scenario #2: N<sub>2</sub> ice deposits in the low-elevated terrains of the northern mid-latitudes,  
 167 as observed by New Horizons [Schmitt et al., 2017; Protopapa et al., 2017].
- 168 • Scenario #3: Same as Scenario #2 but with extra N<sub>2</sub> ice deposits in the non-observed  
 169 southern hemisphere.

170 Figure 1 shows the initial (year 1984) surface ice distribution corresponding to these  
 171 three scenarios as simulated in the GCM (the same distribution is obtained at the end  
 172 of the GCM simulation in 2015 as it does not vary significantly within this time frame).  
 173 Note that all scenarios have a N<sub>2</sub>-free surface below 60°S. No VTM simulation was able  
 174 to reproduce a realistic threefold increase of surface pressure while having N<sub>2</sub> ice deposits  
 175 below 60°S during the 1988-2015 period. Such deposits would induced a strong condensa-  
 176 tion flow and trigger a surface pressure drop around year 2000 [Meza et al., 2019; Bertrand  
 177 et al., 2019].

178 In this paper, we explore these scenarios with the new version of the LMD Pluto GCM,  
 179 with a focus on Sputnik Planitia and the atmospheric circulation. Note that most of the  
 180 previous GCM results shown in Forget et al. [2017] are still valid and are therefore not

181 shown again (for instance, the steady state and the mixing of CH<sub>4</sub> and CO in the atmo-  
182 sphere, the homogeneous atmospheric temperatures, the ubiquity of katabatic winds).

### 3. Near surface winds in Sputnik Planitia

183 In this section, we present the near-surface circulation in Sputnik Planitia obtained in  
184 the high resolution GCM simulations for 2015 and compare the results with the available  
185 observations from New Horizons.

#### 3.1. Model results: anti-clockwise flow and boundary currents

186 In all our GCM simulations, we obtain a near-surface anti-clockwise atmospheric current  
187 that flows over Sputnik Planitia, from its north-east to its south-west side, as shown by  
188 Figure 2.C and Figure 3. What triggers this current? The N<sub>2</sub> ice sheet is Pluto's heart,  
189 beating once every day as N<sub>2</sub> sublimates during daytime and condenses during nighttime. In  
190 2015 (northern spring), Pluto's cardiac activity is relatively high as latitudes located above  
191 38°N (Pluto's current arctic summer, Binzel et al. [2017]) experience constant insolation  
192 across a diurnal cycle, involving large N<sub>2</sub> sublimation rates [Forget et al., 2017]. Most of  
193 the sublimation occurs in the northern part of the ice sheet, under constant illumination,  
194 while most of the condensation occurs in the southern part, close to the winter polar night.  
195 This leads to a net sublimation flow of cold air from the northern to the southern part of  
196 the ice sheet. As the near-surface air flows from northern latitudes toward the equator, it  
197 is deflected westward by the Coriolis effect, like trade winds on the Earth and on Mars.  
198 This explains the dominant westward winds obtained in the northern part of Sputnik  
199 Planitia. Then, as it reaches the high relief western boundary of the basin (defined by  
200 mountain ranges that reach elevations of 5 km above the plains, Figure 2.A), the flow

201 is deviated and follows the boundary down to the southern latitudes of the basin, such  
202 as terrestrial or Martian western boundary currents (WBC, Figure 4, Anderson [1976];  
203 Joshi et al. [1994, 1995]). In the late afternoon, the flow reaches the south-eastern edge of  
204 Sputnik Planitia and is deviated back toward northern latitudes. The western boundary  
205 current is the main artery of the heart-shaped basin, as it transports significant amounts  
206 of air from one hemisphere to another (see Section 4.1.1).

207 We investigated further this anti-clockwise current by performing five new GCM simu-  
208 lations (not shown) similar to the reference case shown by Figure 2.C and Figure 3: (1)  
209 A simulation without  $N_2$  condensation-sublimation produces a completely different cir-  
210 culation with south-to-north clockwise current characterized by much weaker winds (less  
211 than  $1 \text{ m s}^{-1}$ ). (2) A simulation without the diurnal cycle (daily averaged insolation) pro-  
212 duces an anti-clockwise circulation similar to the reference case. (3) A simulation without  
213 the high-relief south-eastern boundary of Sputnik Planitia (i.e. the basin extends to its  
214 south-east margin) produces the same circulation than the reference case but there is no  
215 northward return branch of the flow on the eastern regions (the winds are rushing into  
216 the extended south-east regions of the modified basin). (4) A simulation with a rotation  
217 period of 0 s (no Coriolis forcing) produces no westward deflection of the flow and thus  
218 no boundary current (the sublimation flow is oriented from north to south in the basin).  
219 (5) A simulation with a rotation period of 0.5 Earth days (instead of the real period of  
220 6.387 Earth days) produces a stronger and narrower WBC (more confined to the western  
221 boundary of the basin) than that in the reference case, thus better resembling the WBC  
222 known on Earth and on Mars. The northward return branch of the flow in the eastern  
223 regions of Sputnik Planitia remains relatively unchanged.

224 These investigations further demonstrate that the WBC is forced by the N<sub>2</sub>  
 225 condensation-sublimation flow and the deviation of the flow by the Coriolis force and  
 226 the high-relief boundaries of Sputnik Planitia. This peculiar circulation compares well  
 227 with the WBCs known on Mars and on Earth (they are dynamically equivalent in the  
 228 sense that there is some degree of western intensification). However, note that on Pluto,  
 229 the length scales are different since the WBC is confined in a 3-km deep, 1000-km wide  
 230 basin. The examples of WBC on Mars and on Earth usually correspond to much larger  
 231 areas, if not semi-infinite plans. One can estimate the length scale at which rotational ef-  
 232 fects become significant for meteorological phenomena by calculating the Rossby radius  
 233 of deformation  $R$  on Pluto, given by :

$$R = \frac{(gD)^{0.5}}{f_c} \quad (1)$$

234 Where  $g$  is the gravitational constant,  $D$  is the depth of the atmospheric layer, and  $f_c$   
 235 is the Coriolis parameter. Assuming  $D = 3$  km (the depth of the basin where the near-  
 236 surface flow is simulated), we obtain  $R \sim 4000$  km. The Rossby radius of deformation is  
 237 larger than the Sputnik Planitia basin, which explains why the WBC is not very narrow in  
 238 the reference simulation. The WBC really emerges when we increase the rotation rate: in  
 239 the simulation with a rotation period of 0.5 Earth days, the Rossby radius of deformation  
 240 is decreased by a factor of almost 10 and becomes lower than the length scale of the basin.

## 3.2. Comparisons with possible indicators of aeolian activity on Pluto's surface

### 241 3.2.1. Wind streaks

242 New Horizons observations of Pluto revealed the presence of dark wind streaks located  
243 on the western side of Sputnik Planitia between  $15^{\circ}\text{N}$ - $25^{\circ}\text{N}$  [Stern et al., 2015], and ori-  
244 ented northwest-southeast ( $153\pm 10^{\circ}$ , Figure 2.B inset). As on Mars, the streaks form  
245 an elongated albedo contrast with the surrounding ice plains, slightly darkening the ice  
246 [Thomas et al., 1981; Greeley et al., 1993; Geissler, 2005]. Here they appear to stem  
247 from isolated water ice blocks, which here are sufficiently interior to Sputnik Planitia such  
248 that they may be floating on the  $\text{N}_2$  ice. Modification of wind flow by these topographic  
249 obstacles is interpreted to be the cause of the surface albedo contrast [Stern et al., 2015].  
250 Two separate wind streaks with different orientations sometimes stem from a single block,  
251 which could reflect recent circulation changes. The wind directions and the WBC pre-  
252 dicted by the GCM are consistent with the wind directions derived from these streaks.  
253 Possible scenarios for the formation of the surface albedo contrast are discussed in the  
254 following section and in Section 5.1.

### 255 3.2.2. The westward extended dark plains

256 Sputnik Planitia displays relatively dark plains in its north (above  $30^{\circ}\text{N}$ ) and western  
257 regions, which contrast with the brighter plains in its center, as shown by Figure 2.B. The  
258 difference of albedo between the dark and bright plains is  $\sim 0.05$  [Buratti et al., 2017].  
259 The darker color correlates with a weaker spectral signature of  $\text{N}_2$  and  $\text{CH}_4$ , interpreted  
260 as combination of a decrease of the size of the  $\text{N}_2$ -rich ice grains, but richer in  $\text{CH}_4$ ,  
261 coexisting with a larger amount of  $\text{CH}_4$ -rich ice grains [Schmitt et al., 2017; Protopapa  
262 et al., 2017]. This probably reflects recent  $\text{N}_2$  ice sublimation processes which could form,  
263 according to its binary phase diagram,  $\text{CH}_4$ -rich grains from the saturation of  $\text{CH}_4$  diluted  
264 in the  $\text{N}_2$ -rich ice. This is supported by simulations performed with the Pluto VTM,

265 showing that the latitudes north of  $15^{\circ}\text{N}$  experienced a net loss of  $\text{N}_2$  ice during the 2000-  
266 2015 period [Bertrand et al., 2018], whereas latitudes south of  $15^{\circ}\text{N}$  experienced a net  
267 deposition. In 2015, the sublimation rate is especially high north of  $38^{\circ}\text{N}$ , which presently  
268 experiences constant illumination, explaining the much lower albedo of the plains located  
269 there. White et al. [2017] noted that the boundary between the dark and bright plains is  
270 located at  $30^{\circ}\text{N}$ , which corresponds to the Arctic Circle (the southernmost latitude that  
271 can experience continuous insolation over a diurnal period at least once during an orbit).  
272 They hypothesized that net sublimation north of  $30^{\circ}\text{N}$  is revealing and concentrating  
273 darker, older, dark material-infused ice that forms the bulk of the  $\text{N}_2$  ice filling the Sputnik  
274 Planitia basin, while net condensation south of  $30^{\circ}\text{N}$  is depositing a thin veneer of fresh,  
275 bright  $\text{N}_2$  ice onto the plains and onto the bright pitted uplands of east Tombaugh Regio  
276 (Figure 2.B). A similar process may be occurring at Triton’s south pole, where sublimation  
277 of ices may be concentrating dark organic matter on the surface of the ice or exposing  
278 layers of this material which have built up in the ice over many seasonal cycles [Stansberry  
279 et al., 1989].

280 However, the band of dark plains extending south of  $30^{\circ}\text{N}$  down the western margin  
281 of Sputnik Planitia indicates that factors besides latitude-dependant insolation are also  
282 influential in defining the albedo contrast in the plains, and the observation of wind streaks  
283 here suggests that near-surface winds may play a role. Our GCM results are consistent  
284 with the hypothesis that eolian activity is uncovering dark plains in this western region  
285 of Sputnik Planitia, as the sublimation flow and the WBC obtained in our simulations  
286 produce windier conditions roughly above the dark plains, Figure 2.C. However, the exact

287 mechanisms leading to an increase of sublimation or erosion at these dark plains remain  
 288 uncertain. We discuss possible scenarios in Section 5.1.

## 4. General circulation regime on Pluto

289 In this section, we explore the general circulation regime obtained with the high reso-  
 290 lution GCM simulations for 2015, for the three reference scenarios. We also present for  
 291 the first time a low resolution GCM simulation performed over three entire Pluto years,  
 292 and we describe the seasonal evolution of the circulation regime.

### 4.1. General circulation in 2015 from high resolution GCM runs

#### 293 4.1.1. Meridional circulation

294 Figure 5 shows the zonally-averaged meridional mass stream functions and zonal winds  
 295 obtained for 2015 in each GCM simulation. There are few differences between the three  
 296 scenarios. In the lowermost atmospheric scale height (below 20 km altitude), the zonal  
 297 mean meridional circulation is characterized by a flow from the northern to the southern  
 298 latitudes, which is controlled by the sublimation-condensation flow of  $N_2$  inside Sputnik  
 299 Planitia and outside when mid-latitudinal  $N_2$  deposits are present (scenarios #2 and #3).  
 300 This is shown by the anti-clockwise circulation cells (left column on Figure 5), which  
 301 remain open near the surface (there is no return branch) because of the net transport of  
 302  $N_2$  from the summer hemisphere (sublimation) to the winter hemisphere (condensation).  
 303 Most of this near-surface meridional flow is controlled by the WBC, described above, which  
 304 only occurs in Sputnik Planitia. This current efficiently forces N-S meridional transport  
 305 of  $N_2$  within the first scale height (which is eventually strengthened by the presence of  
 306 mid-latitude  $N_2$  deposits).

307    Above 20 km, the zonal mean meridional circulation is also dominated by an anti-  
308 clockwise circulation in some cases, centered above the subsolar point and controlled  
309 by thermal gradients in the atmosphere. This thermal cell is not present in all three  
310 simulation cases. Note that the meridional circulation in the upper atmosphere remains  
311 weak at all longitudes, with winds lower than  $1 \text{ m s}^{-1}$ . If the zonally averaged meridional  
312 circulation is dominated by a southward flow, this is not true at all longitudes and  
313 altitudes. Figure 6 shows the meridional air mass flow averaged between  $45^\circ\text{S}$ - $45^\circ\text{N}$  for  
314 different ranges of altitudes. In the lowest 5 km of the atmosphere (blue curves), most  
315 of the cross-equatorial transport of air occurs around longitude  $180^\circ$ , that is in Sputnik  
316 Planitia. The basin is an efficient channel to transport freshly-sublimed air, gaseous  
317 methane and other atmospheric constituents from one hemisphere to the other (in 2015  
318 the transport is mostly from north to south). The two peaks at longitude  $\sim 170^\circ$  and  
319  $\sim 190^\circ$  correspond to the southward flow and northward flow respectively associated with  
320 the western boundary current and the northward return branch of the flow, as shown on  
321 Figure 3.

322    In simulation #1, the cross-equatorial transport of air is mostly directed southward be-  
323 low 20 km but is balanced by northward currents above 20 km, at longitudes  $\sim 120^\circ$   
324 and  $\sim 330^\circ$ . In simulation #3, the presence of mid-litudinal deposits reinforces the  
325 sublimation-condensation flow and the cross-equatorial transport of air is mainly south-  
326 ward transport (in particular, the condensation at southern latitudes prevent northward  
327 return flow of air). This result can be compared with pre-New Horizons GCM predictions  
328 published by Toigo et al. [2015], which assumed that  $\text{N}_2$  ice was covering both poles.  
329 This is also seen on Figure 5, showing small clockwise cells at high northern and southern

latitudes in simulation #1. When mid-latitude N<sub>2</sub> ice deposits are present (Scenarios #2 and #3), the N-S meridional flux is strengthened and does not allow the formation of the clockwise cells.

#### 4.1.2. Zonal circulation

The zonally averaged meridional flux is weak but is still sufficient to trigger westward winds at all latitudes, by conservation of angular momentum as the N<sub>2</sub> molecules are transported from one hemisphere to the other and move away from the rotation axis as they cross the equator (as shown by the red cells on Figure 5). Thus, we find that the general circulation of Pluto's atmosphere is dominated by a retro-rotation, with zonal westward winds reaching 8-13 m s<sup>-1</sup> at altitudes 20-250 km. The wind amplitude decreases toward the poles, but the winds remain directed westward (e.g. 4 m s<sup>-1</sup> westward winds are obtained at the mid-latitudes between 50 and 200 km altitude). This result is independent of the presence of mid-litudinal N<sub>2</sub> ice deposits outside Sputnik Planitia, which do not significantly change the circulation regime. In fact, they provide an extra source of sublimated N<sub>2</sub> in the northern hemisphere and an extra condensation sink of N<sub>2</sub> in the southern hemisphere and therefore strengthen the cross equatorial transport of N<sub>2</sub> and the westward winds.

In Forget et al. [2017], Pluto's general circulation was shown to be extremely sensitive to the surface distribution of N<sub>2</sub> ice. In this paper, we show that it is not the case if we assume that N<sub>2</sub> ice fills Sputnik Planitia and eventually the mid-latitudes but not the poles. The critical new factor in the GCM is the better representation of the Sputnik Planitia basin, which is more extended toward southern latitudes than was assumed before. In the simulations performed by Forget et al. [2017], the basin was modeled by a circular

353 crater located between  $0^{\circ}\text{N}$  and  $45^{\circ}\text{N}$ , while in reality, it extends southward down to  $25^{\circ}\text{S}$ .  
354 In our new GCM simulations, presented in this paper, there is therefore an unavoidable  
355 cross-equatorial transport of  $\text{N}_2$  from its northern (sublimation-dominated) to its southern  
356 (condensation-dominated) part, which is sufficient to trigger westward winds in the upper  
357 atmosphere by conservation of angular momentum. Note that if we place a  $\text{N}_2$  ice deposit  
358 at the south pole in 2015, then we obtain a prograde jet around the south pole, with  
359 eastward winds up to  $5 \text{ m s}^{-1}$ , while the retro-rotation remains dominant at other latitudes  
360 (Figure not shown). If the condensation flow toward the south pole is very strong, then  
361 momentum can be transferred from the pole to the equator through wave instability  
362 mechanisms, and trigger a super-rotation in Pluto's atmosphere, as shown in Fig.10b of  
363 Forget et al. [2017].

364 However, a scenario with  $\text{N}_2$  condensation at the south pole is unrealistic for 2015.  
365 Surface pressure is currently increasing on Pluto, which suggests limited  $\text{N}_2$  condensation  
366 in the southern winter hemisphere. In fact, if  $\text{N}_2$  ice was covering the south pole, then the  
367 peak of surface pressure should have occurred around year 2000, according to the models  
368 [Bertrand et al., 2018, 2019; Meza et al., 2019]. The absence of  $\text{N}_2$  ice deposits at the  
369 south pole during the 1988-2015 period (early northern spring) could be explained by a  
370 combination of (1) the high thermal inertia of the substrate, which would enable the south  
371 pole to store the heat accumulated during previous summer and release it during fall and  
372 winter, thus preventing  $\text{N}_2$  condensation at the pole during this period [Bertrand et al.,  
373 2018], (2) the presence of high-elevated terrains at the south pole, and (3) a darker surface  
374 albedo at the south pole, induced by a long period of sublimation (previous southern

375 summer) of the surface ices ( $N_2$ ,  $CH_4$ ) which would lead to the exposure of more dark red  
376 materials.

377 To conclude, the assumption that Pluto's general circulation is sensitive to the surface  
378 distribution of  $N_2$  ice remains true, but our model strongly suggests a circulation regime  
379 dominated by a retro-rotation for 2015, assuming realistic distributions for  $N_2$  ice. In  
380 addition, the WBC in Sputnik Planitia is present in all simulation cases. However, al-  
381 though the overall meridional flow pattern remains southward (in the zonal average) in  
382 all simulation cases, some variability in meridional transport is obtained, depending on  
383 the location of the  $N_2$  ice reservoirs.

#### 384 4.1.3. Thermal tides and waves

385 The solar-induced sublimation breathing from the surface  $N_2$  ice deposits triggers atmo-  
386 spheric thermal tides that could explain the density fluctuations observed during stellar  
387 occultations of Pluto's atmosphere [Elliot et al., 2003; Person et al., 2008; Toigo et al.,  
388 2010; Forget et al., 2017]. In particular, the  $N_2$  breathing in Sputnik Planitia is a strong  
389 and very localized perturbation of Pluto's atmosphere. As in Forget et al. [2017], we  
390 obtained thermal tides structures in the temperature profile of our high-resolution GCM  
391 simulations, shown by Figure 7. The properties of the thermal tides are very similar to  
392 the predictions presented in Forget et al. [2017] (with no south pole  $N_2$  condensation),  
393 including (1) temperature variations of up to 0.1 K and 0.2 K for scenarios #1 and #3  
394 respectively, (2) wavenumber = 1 tides with a 10-20 km vertical wavelength below 100 km  
395 and a longer wavelength above.

396 Signatures of other types of waves are also present in our GCM simulations. For in-  
397 stance, barotropic wave activity is seen, similar to that shown in Forget et al. [2017] in

398 the case with south pole N<sub>2</sub> condensation, but with a much lower intensity. In addition,  
399 vertical motions are induced by the topography, in particular in the surroundings of Sput-  
400 nik Planitia, and could lead to orographic gravity waves in the atmosphere. However, the  
401 horizontal, vertical, and time resolution of our simulations are not ideal to investigate and  
402 analyze these wave mechanisms in detail. Consequently, we reserve this study for a future  
403 work which will involve improved GCM simulations (e.g. with more constraints on N<sub>2</sub> ice  
404 surface distribution) and wave analysis tools.

## 4.2. Evolution of the circulation regime over an entire Pluto year

405 In this section, we explore how the general circulation of Pluto’s atmosphere varies over  
406 the year, as seasonal N<sub>2</sub> deposits form or disappear in both hemispheres. We extended  
407 the GCM simulation at relatively low resolution ( $11.25^\circ \times 7.5^\circ$ ) from Earth year 1984 to  
408 year 2732, that is 3 entire Pluto years.

409 The initial state corresponds to Scenario #3, with mid-latitudinal bands of N<sub>2</sub> deposits.  
410 Here we focus only on the annual evolution of the atmospheric circulation. The detailed  
411 analysis of this multi-year Pluto simulation and associated sensitivity studies will be  
412 performed in a future work, mostly because more years are necessary to reach a perfectly  
413 balanced CH<sub>4</sub> cycle. Figures 8 and 9 show the zonal mean zonal winds obtained at 20  
414 and 100 km respectively, whereas the bottom panel of Figure 8 shows the 3-year evolution  
415 of the zonal mean distribution of N<sub>2</sub> ice. In this simulation, there is few seasonal N<sub>2</sub> ice  
416 deposits at the poles, and the pressure cycle is similar to the cycles obtained in previous  
417 works [Bertrand and Forget, 2016; Bertrand et al., 2018, 2019]. We note that although  
418 the simulation is close to steady state, the results from the first year are slightly different

419 from those from the second and third year. Consequently, we consider the first year as  
420 spin up time and we only analyze the third year.

421 We find that the retro-rotation at 20 km is maintained during most of Pluto's year,  
422 with a maximum westward wind of  $\sim 10\text{-}12\text{ m s}^{-1}$  centered above Sputnik Planitia. This  
423 is because there is always enough cross-equatorial transport of gaseous  $\text{N}_2$  in Sputnik  
424 Planitia (and outside), from north to south in northern spring and summer or south to  
425 north during the opposite season. Around  $L_s=270\text{-}300^\circ$  (southern summer), the zonal  
426 winds at this altitude are still directed westward but are significantly weaker. This is due  
427 to the larger extent of the ice sheet in the northern, compared to the southern, hemisphere  
428 (Sputnik Planitia is not symmetrical about the equator). Because of this asymmetry,  
429 the sources of  $\text{N}_2$  are weaker than the sinks of  $\text{N}_2$  during  $L_s=270\text{-}300^\circ$ , and significant  
430 meridional transport during this period occurs in the northern part of the ice sheet, as  
431 shown by Figure 10. In other words, the cross-equatorial transport of gaseous  $\text{N}_2$  from the  
432 southern to the northern part of the ice sheet is much weaker during this season, hence  
433 the weaker winds. Note that if large amounts of  $\text{N}_2$  are still covering the southern summer  
434 hemisphere during this period, the retro-rotation would be strengthened. Interestingly,  
435 the retro-rotation is currently at its highest intensity, because the subsolar point is at  
436  $\sim 50^\circ\text{N}$  and there is preferential sublimation of  $\text{N}_2$  from the mid-latitudinal deposits and  
437 from the northern part of Sputnik Planitia. Another maximum is obtained around year  
438 2150 (Solar longitude  $L_s=218^\circ$ ) when the subsolar point is above the latitude  $\sim 33^\circ\text{S}$  and  
439 the southern  $\text{N}_2$  deposits are preferentially sublimating.

440 Figure 9 shows similar results at 100 km altitude. The retro-rotation in the upper  
441 atmosphere is maintained during most of Pluto's year. Note that the strongest winds

442 are centered above Sputnik Planitia, and that the weaker winds are obtained at the  
 443 equinoxes. A stronger prograde jet is obtained in the north hemisphere at 40°N during  
 444 northern winter ( $L_s=270-315^\circ$ ). Figure 11 shows the zonal mean zonal winds obtained  
 445 during this period. The prograde jet in the upper atmosphere results from the intense  
 446 poleward  $N_2$  condensation flow and the conservation of angular momentum. The figure  
 447 also shows that the circulation can quickly switch from retrograde to prograde over a  
 448 Pluto year.

## 5. Discussions

449 Despite different  $N_2$  ice distribution, the three reference GCM simulations of this paper  
 450 are characterized by the same circulation regime in 2015, that is an anti-clockwise current  
 451 in Sputnik Planitia and a retro-rotation with  $\sim 10 \text{ m s}^{-1}$  westward winds in the upper  
 452 atmosphere. In this section, we explore the possible impact of this circulation on Pluto's  
 453 surface and geology.

### 5.1. Possible eolian processes impacting the surface ice

#### 454 5.1.1. Effect of downward sensible heat flux

455 In this section, we evaluate the sensible heat flux above Sputnik Planitia (controlled by  
 456 the temperature gradient and the near-surface atmospheric motions) and how it affects  
 457 the  $N_2$  ice albedo and composition. In the GCM, the sensible heat flux is calculated using  
 458 the bulk aerodynamic formula:

$$H_s = \rho C_p C_d V_1 (T_s - T_{z1}), \quad (2)$$

459 where  $(T_s - T_{z_1})$  is the temperature difference between surface and atmosphere at altitude  
 460  $z_1$  above the surface (in the model, the first atmospheric layer is at  $z_1 = 5$  m),  $C_d =$   
 461  $[0.4 / \ln(z_1 / z_0)]^2$  is the von Karman drag coefficient depending on the surface roughness  $z_0$   
 462 (assumed to be 1 cm everywhere),  $\rho$  is the near surface air density ( $\sim 10^{-4}$  kg m $^{-3}$  in 2015),  
 463  $C_p$  is the atmospheric specific heat capacity (1000 J kg $^{-1}$  K $^{-1}$ ) and  $V_1$  is the horizontal  
 464 wind speed at altitude  $z_1$ . Above Sputnik Planitia, the sensible heat flux transferred to  
 465 the surface would be consumed through the latent heat of sublimation of N $_2$  ice and the  
 466 maintenance of vapor pressure equilibrium. This can be approximated by:

$$H_s = L \frac{dM}{dt}, \quad (3)$$

467 where  $L$  is the latent heat of sublimation of N $_2$  ice ( $2.5 \times 10^5$  J Kg $^{-1}$ ),  $M$  is the mass of  
 468 N $_2$  ice and  $t$  is time. According to the model, N $_2$  sublimation injects cold air into the atmo-  
 469 sphere above Sputnik Planitia, leading to a weak thermal gradient  $T_s - T_1$  and therefore a  
 470 negligible surface heat flux during daytime. However, during nighttime, katabatic winds  
 471 transport the near-surface air from the surrounding terrains towards Sputnik Planitia,  
 472 filling the basin with an air warmer (43-46 K at 5 m) than the surface, which remains at  
 473 the equilibrium temperature ( $\sim 37$  K). This thermal gradient leads to a downward sensible  
 474 heat flux that warms the surface and limits nighttime N $_2$  condensation.

475 Assuming  $|T_s - T_1| = 9$  K and  $V_1 = 3$  m s $^{-1}$ , we find that the downward sensible  
 476 heat flux in Sputnik Planitia can reach 11 mW m $^{-2}$  during nighttime, which is significant  
 477 since the radiative flux  $\epsilon \sigma T^4$  is only 85 mW m $^{-2}$  (when  $T = 37$  K and  $\epsilon = 0.8$ ). Hence  
 478 the mass of N $_2$  condensing at night in Sputnik Planitia is significantly impacted by the  
 479 sensible heat flux. This quantitative energy balance calculation shows, to first order, that

480 the sensible heat flux cannot be systematically neglected in the surface energy budget  
481 despite the low density of the Plutonian atmosphere.

482 Our simulations show an enhancement of nighttime downward sensible heat flux along  
483 the northern and western boundary of Sputnik Planitia (Figure 12.A-B), because winds  
484 are stronger there (following the western boundary current and the anti-clockwise near-  
485 surface circulation) and because warmer air is injected at night from the surrounding  
486 dark material-covered slopes and terrains. This correlates to the darker plains of Sputnik  
487 Planitia and could play a role in changing the sublimation rates in these regions. In fact,  
488 there seems to be a pattern whereby the darkest plains in the mid-western part of Sputnik  
489 Planitia tend to be proximal to tall mountains, which could be explained by the larger  
490 sensible heat flux, induced by the downslope transport of warmer air from the top of these  
491 mountains to the plains by stronger katabatic winds.

492 In general, the model predicts that the near surface air injected at night into the western  
493 side of Sputnik Planitia remains  $\sim 3$  K warmer than the air injected into the center of  
494 the ice sheet. Combined with stronger winds due to the WBC, we find that the western  
495 terrains of the ice sheet could have lost, in 2015, about 10% more  $N_2$  ice than the central  
496 terrains (about 3 mm). This mechanism could have occurred continuously over the last  
497 15 years, as the  $N_2$  ice condensation-sublimation rates and the near-surface circulation  
498 remained relatively unchanged during this period, according to the model [Bertrand et al.,  
499 2018]. In this case, the difference in ice loss between the western and central plains would  
500 reach  $\sim 45$  mm. Consequently, the action of downward sensible heat flux seems to be a  
501 possible process to explain the increase in  $N_2$  sublimation in the western regions of Sputnik  
502 Planitia, as inferred from New Horizons observations. This process could induce a decrease

503 in surface albedo which would lead to an amplifying positive feedback by increasing the  
504 absorption of incoming radiation and thus the sublimation rate (see Section 5.1.6).

### 505 **5.1.2. Effect of mechanical erosion**

506 Enhanced sublimation or mechanical erosion of N<sub>2</sub> ice by the winds over the ice sheet  
507 could help disrupt the ice, as has been suggested for the polar caps of CO<sub>2</sub> on Mars  
508 [Appéré et al., 2011; Spiga et al., 2011]. Our model results could support this idea, since  
509 the WBC induces stronger winds and therefore higher near-surface stress above the dark  
510 plains of Sputnik Planitia (Figure 12.C). However, because of Pluto’s low surface pressure,  
511 the surface stress obtained with the GCM in these regions is of the order of  $\mu\text{N m}^{-2}$ , which  
512 is very low (100-1000 times weaker than on Mars). This does not appear to be enough  
513 to significantly darken the ice by erosion of N<sub>2</sub> ice and subsequent accumulation of dark  
514 materials, even if such a surface stress occurred continuously over the last 15 Earth years.  
515 Note that the erosion of N<sub>2</sub> ice could have helped forming a CH<sub>4</sub>-rich layer on top of  
516 the surface and impact the spectrum of the surface, but it would also probably lead to a  
517 brighter surface as small CH<sub>4</sub> ice grains form above large transparent N<sub>2</sub> ice grains.

### 518 **5.1.3. Effect of surface accumulation of haze particles**

519 In this section we investigate how N<sub>2</sub> ice reservoirs impact the accumulation of haze  
520 particles onto Pluto’s surface, and we examine the accumulation of haze particles in  
521 Sputnik Planitia as a process that is potentially responsible for the observed contrasts of  
522 color and composition on the surface of the ice sheet.

523 We have run the GCM with the haze parameterization described in Bertrand and Forget  
524 [2017], which reproduces to first order the photolysis of CH<sub>4</sub> molecules in the upper  
525 atmosphere by Lyman- $\alpha$  UV radiation, the production of gaseous haze precursors, and

526 their conversion into solid particles (using a simple conversion scheme with a characteristic  
527 time for aerosol growth set to  $10^7$  s). In the model, the haze particles are passive tracers  
528 with a fixed uniform radius that only affects their sedimentation velocity. Although this  
529 parameterization is relatively simplified and not well validated, it remains reasonable to  
530 use it here to investigate the transport of haze particles by the circulation. As shown in  
531 Bertrand and Forget [2017], haze production in the upper atmosphere above the north pole  
532 in 2015 is more abundant than that at lower latitudes (because of constant illumination  
533 and thus constant  $\text{CH}_4$  photolysis), and the modeled haze is more extensive in the northern  
534 hemisphere because the meridional circulation (and therefore the southward transport of  
535 haze particles) is relatively weak.

536 Figure 13 shows a global map of net surface haze accumulation as obtained with the  
537 low-resolution GCM simulation (Scenario #2) over the period 1984-2015, assuming 10 nm  
538 haze particles. The distribution of haze particles settling onto the surface is significantly  
539 impacted by  $\text{N}_2$  condensation and sublimation flows. This is especially true for particles  
540 with a small sedimentation radius, such as 10 nm particles, which have a low sedimentation  
541 velocity (e.g.  $4.6 \times 10^{-4}$  m s $^{-1}$  at 1 Pa near the surface).

542 The simulation shows that these particles are repelled from the surface of the plains by  
543  $\text{N}_2$  sublimation flows and drawn towards the surface by  $\text{N}_2$  condensation flows and the  
544 katabatic winds [see Fig. 12 in Bertrand and Forget, 2017]. Whereas  $\text{N}_2$  ice reservoirs  
545 located in the polar night continuously attract haze particles as well as  $\text{N}_2$ , those located  
546 in the polar day continuously repel haze particles. In the diurnal zone, daytime sublima-  
547 tion and nighttime condensation occur, but the condensation is much more efficient at  
548 attracting haze particles than sublimation is at repelling them. This is because  $\text{N}_2$  ice is

549 locally distributed in depressions [Bertrand and Forget, 2016], with katabatic winds on  
550 the surrounding slopes balancing daytime-induced sublimation flows and strengthening  
551 nighttime-induced condensation flows.

552 Consequently, according to the model, significant accumulation of haze particles could  
553 have occurred in low-latitude  $N_2$  ice reservoirs over the period 1984-2015. The model  
554 predicts less accumulation in the reservoirs north of  $38^\circ N$ , which experienced constant  
555 illumination in 2015. In particular, the model suggests that the accumulation of haze par-  
556 ticles could be up to 10 times larger in depressions containing  $N_2$  ice than elsewhere. The  
557 haze accumulation predicted by the model is even larger in the southern regions of Sputnik  
558 Planitia, where the strong katabatic winds and intense condensation flows occurred during  
559 the 1984-2015 period. Note that Grundy et al. [2018] estimated that atmospheric haze  
560 particles compose 1.4% of Sputnik Planitia's present-day bulk, by assuming a uniform  
561 haze deposition rate across Pluto's surface. Here our modeling results suggest a larger  
562 fraction by a factor of up to 10 within the low-latitude  $N_2$  ice reservoirs.

563 Figure 13 also shows larger haze accumulation in the north-western regions of Sputnik  
564 Planitia than in the north-eastern regions, by a factor of 3 in the plains and 6 on the  
565 outermost edges, according to the model. This is consistent with Schmitt et al. [Fig. 35  
566 in 2017], which shows an increasing amount of red material in the north-western regions  
567 of Sputnik Planitia. Interestingly, in this figure the pattern of distribution of the red  
568 material is very similar to the wind pattern at its strongest during Pluto year, around  $L_s$   
569  $= 225^\circ$ , in Figure 10. At this period very strong N-E winds blow from Cthulhu Macula  
570 and may lift and transport haze particle accumulated at the surface of this region (still

571 highly mobile, as not included in ice) and deposit them at the surface of the N-W part of  
572 Sputnik Planitia.

573 In our simulation, the difference in ice contamination by haze particles across Sputnik  
574 Planitia is significant and could potentially be sufficient to impact the surface albedo by  
575 a few percents (and thus the sublimation-condensation rates) and lead to the observed  
576 contrasts of color and composition in Sputnik Planitia. This increased amount of impu-  
577 rities could also impact the ice rheology. Here the haze accumulation is mostly driven  
578 by the condensation flow, the strong katabatic winds in the western regions and by the  
579 near-surface circulation within Sputnik Planitia, although the low horizontal resolution  
580 of the global simulation may be too coarse here to properly represent the near-surface  
581 circulation.

582 Figure 12.D shows the net accumulation of haze particles in Sputnik Planitia over  
583 one Pluto day in 2015, modeled using the high-resolution GCM simulation. In 2015, the  
584 intense  $N_2$  sublimation flow and the WBC north of Sputnik Planitia tend to repel the haze  
585 particles during daytime. However, at night, the condensation flows coupled to katabatic  
586 winds are efficient to put large amounts of particles onto the  $N_2$  ice plains surrounding  
587 the Al-Idrisi, Zheng He, Barè and Hillary Montes. The haze accumulation patterns on  
588 Figure 12.D can be compared to the observations of dark plains in these regions, although  
589 we note that there are still expanses of bright plains here and that the boundaries between  
590 bright and dark plains tend to be more abrupt than what the simulation produces. We  
591 also note that haze accumulation is predicted in the eastern regions by the model, which is  
592 not supported by the observations showing that the plains of these regions remain bright.

593 In the southern regions of Sputnik Planitia, the haze particles could probably be quickly  
594 buried by the diurnal accumulation of N<sub>2</sub> ice, allowing the plains of these regions to remain  
595 bright. Our simulated haze deposition rates are stronger inside southern Sputnik Planitia  
596 than outside but remain of the order of 10<sup>-8</sup>-10<sup>-7</sup> kg m<sup>-2</sup> per Pluto day, that is much  
597 below the N<sub>2</sub> deposition rates, which are of the order of 10<sup>-1</sup> kg m<sup>-2</sup> per Pluto day at  
598 this latitude and season (100-200 μm, see Figure 16). The high N<sub>2</sub> deposition rates in  
599 southern Sputnik Planitia should be sufficient to mask the haze particles accumulating  
600 in this region and prevent discoloration of the ice, in agreement with the observed bright  
601 surface of the southernmost plains of the ice sheet. To conclude, the transport of haze  
602 particles by the circulation seems to be a possible mechanism to trigger ice composition  
603 and color contrasts across Sputnik Planitia, although it remains difficult to assess with the  
604 model and the simplified haze parameterization.

#### 605 **5.1.4. Dark materials ejected from the dark troughs of Sputnik Planitia**

606 At the northern edge of Sputnik Planitia, dark convective cells boundaries seem to  
607 correspond to troughs filled with dark materials [White et al., 2017]. The very dark plains  
608 observed in this region seem to be located around these dark troughs. Are dark materials  
609 blown away from these troughs as N<sub>2</sub> sublimates, thus darkening Sputnik Planitia? In  
610 order to test this hypothesis, we added in the model a source of dark material roughly  
611 at the location of the very dark plains (above 40°N in Sputnik Planitia). The material is  
612 injected into the atmosphere during daytime, and is proportional to the sublimation rate  
613 of N<sub>2</sub>.

614 Figure 14 shows how this material is spread into the atmosphere and Figure 15 shows  
615 the net surface accumulation obtained after three days following the first injection. The

616 material is transported by the WBC from the northern to the southern latitudes of Sputnik  
617 Planitia. A larger surface accumulation of the material is found in the western regions  
618 of Sputnik Planitia, in good agreement with the observed location of the dark plains.  
619 Consequently, If large amounts of materials can be mobilized in the northern edge of  
620 Sputnik Planitia (from the dark troughs) as N<sub>2</sub> ice sublimates, they could accumulate in  
621 the north-western regions of Sputnik Planitia and trigger an albedo contrast such as  
622 observed by New Horizons.

### 623 **5.1.5. Transport of ice grains**

624      Could the contrast of color and composition observed in Sputnik Planitia also be due to  
625 transport of ice grains by the near-surface winds and the WBC? For instance, sublimation  
626 of a transparent granular ice layer could raise N<sub>2</sub> ice particles aloft, which could then be  
627 transported by the near-surface winds. Such particles may not sublimate quickly due to  
628 adiabatic cooling in the boundary layer [Hinson et al., 2017]. Alternatively, CH<sub>4</sub> rich  
629 particles mixed with N<sub>2</sub> could also be raised aloft very easily by the N<sub>2</sub> sublimation flow.  
630 This process has been suggested for the formation of dunes west of Sputnik Planitia  
631 [Telfer et al., 2018]. However, the observed dunes, thought to be composed of CH<sub>4</sub>-rich  
632 ice particles, seem to correspond to brighter areas on the ice sheets surface and therefore  
633 cannot explain the observation of bright N<sub>2</sub>-rich or dark CH<sub>4</sub>-rich surface. In addition,  
634 the size of the CH<sub>4</sub> ice grains in Sputnik Planitia seem to be of the order of 1 mm [see  
635 Fig. 4.B in Protopapa et al., 2017], which is too large to be transported by Plutos winds  
636 and saltation processes [Telfer et al., 2018]. Consequently, the transport of ice grains by  
637 the near-surface circulation seems unlikely to be related to the albedo contrast observed  
638 between the dark and bright plains of Sputnik Planitia.

### 639 5.1.6. Surface albedo feedback

640 Albedo and composition positive feedbacks could take place to further increase the  
 641 sublimation rate of  $N_2$  ice over the dark plains. For instance, the difference of sensible  
 642 heat flux over bright and dark plains could have triggered an albedo difference, which  
 643 then could have amplified with time. We can roughly estimate the sublimation rate of  $N_2$   
 644 by neglecting the internal heat flux and the sensible heat flux from the atmosphere and  
 645 write the daytime surface energy balance as:

$$\epsilon\sigma T^4 = (1 - A)F - L\frac{dM}{dt}, \quad (4)$$

646 where  $F$  is the incoming solar flux ( $1 \text{ W m}^{-2}$ ),  $A$  is the  $N_2$  surface albedo,  $T$  is the  
 647 surface temperature ( $\sim 37 \text{ K}$ ),  $\epsilon$  is the ice emissivity ( $\sim 0.8$ ) and  $\sigma$  is the Stefan-Boltzmann  
 648 constant. By assuming a  $N_2$  ice albedo of 0.7 for the bright plains and 0.65 for the dark  
 649 plains, we find differences in sublimation rate of 20%. By assuming albedos of 0.9 and  
 650 0.85, the difference increases up to a factor 4. This would correspond to a difference of  
 651 sublimated thickness of  $N_2$  ice of 30-60  $\mu\text{m}$  over one Pluto day and 25-50 mm over the  
 652 last 15 Earth years. Figure 16 shows the net budget of  $N_2$  ice obtained over one Pluto  
 653 day in 2015 in the reference case using an uniform albedo for  $N_2$  ice and in the case of  
 654 a lower albedo in the northern and western regions of Sputnik Planitia. Between  $5^\circ\text{N}$ -  
 655  $25^\circ\text{N}$ , the slightly lower albedo of  $N_2$  ice in the western regions of Sputnik Planitia is  
 656 enough to invert the net surface energy balance and lead to a net diurnal loss of  $N_2$  ice in  
 657 these regions, whereas the bright central and eastern regions remain dominated by a net  
 658 accumulation of  $N_2$  ice.

659    To conclude, a strong contrast in sensible heat flux at night and the transport of dark  
660 material from a source located in the northern plains (and eventually erosion, haze de-  
661 position, ice grains transport, or another mechanism not mentioned in this paper) could  
662 have triggered an albedo contrast between the north-western and central plains of Sputnik  
663 Planitia. The cumulative effects of these mechanisms and the increased sunlight absorp-  
664 tion by the darker surface seems to be sufficient to keep the energy balance positive and  
665 the surface sublimating in the western regions. This would allow further accumulation of  
666 dark material right at the surface, thus providing an additional positive albedo feedback  
667 to further limit any condensation in these regions.

#### 668    **5.1.7. Difference of ice thickness between the bright and dark plains**

669    The plains of Sputnik Planitia are covered by polygonal cells, thought to be formed by  
670 convective motion of the ice within the ice sheet [McKinnon et al., 2016]. The edges of  
671 the cells appear to be depressed by few tens of meters relative to the centers. Around  
672 30°N, the edges of the convective cells located within the dark plains remain relatively  
673 bright. This suggests a larger accumulation of N<sub>2</sub> ice along the depressions and valleys of  
674 the cells, with a resemblance to terrestrial snow subsisting during spring in the talwegs  
675 and valley paths. This accumulation could be triggered by winds or by less incoming  
676 insolation because of the topographic slopes.

677    Given the spatial extent (~50 km) and homogeneity of these areas, it is reasonable  
678 to assume that the difference in N<sub>2</sub> ice sublimation underlying the origin of the color  
679 and composition contrasts involved an ice thickness of the order of at least a metre.  
680 In this paper, we have explored mechanisms involving the conductive heat flux from the  
681 atmosphere, the erosion of the ice induced by wind stress, the transport of ice grains, haze

682 and dark material by near-surface winds and albedos positive feedbacks. The convective  
683 heat flux, the albedo positive feedback and the transport of dark material seem to be  
684 more efficient to trigger the observed contrasts between bright and dark plains. However,  
685 we estimate that they would involve a difference in sublimated ice thickness of the order  
686 of tens of millimeter over the last 15 years. Consequently, the observed contrast may have  
687 formed over longer timescales, involving these mechanisms over many plutonian years for  
688 instance.

## 5.2. Impact of the retro-rotation on the formation of the Bladed Terrain and Cthulhu Macula

689 A striking longitudinal asymmetry observed on Pluto by New Horizons is the presence  
690 of the CH<sub>4</sub>-rich Bladed Terrain east of Sputnik Planitia, while the uplands of Cthulhu  
691 Macula to the southwest of the ice sheet are mostly volatile-free and covered by a thick  
692 mantle of dark red material, probably several meters thick. The atmospheric retro-rotation  
693 could play a role in the processes leading to this asymmetry. For instance, during periods  
694 of equatorial accumulation of CH<sub>4</sub> ice, the retro-rotation and the injection of cold N<sub>2</sub>-rich  
695 air from Sputnik Planitia could transport and push gaseous CH<sub>4</sub> westward, so that it  
696 favors the accumulation of CH<sub>4</sub> ice at the westernmost longitudes (that is, east of Sputnik  
697 Planitia) leading to the formation of the Bladed Terrain there. A very small difference in  
698 accumulation between east (Cthulhu) and west (Tartarus Dorsa) longitudes could have  
699 been sufficient at first to trigger this asymmetry, because CH<sub>4</sub> ice accumulation in the west  
700 and haze accumulation darkening the surface of Cthulhu in the east would induce very  
701 efficient positive amplifying feedbacks strengthening these resurfacing processes [Earle  
702 et al., 2018]. As CH<sub>4</sub> ice accumulates, it would form large deposits at high altitude,

703 leading another positive feedback between CH<sub>4</sub> condensation and altitude, assuming that  
704 CH<sub>4</sub> preferably condenses at high altitude in the equatorial regions (this is based on New  
705 Horizons observations, see Moore et al. [2018]). Of course, if the water ice bedrock already  
706 formed an asymmetry of altitude at the current location of Cthlhu and the Bladed Terrain,  
707 that may have been sufficient to accumulate CH<sub>4</sub> ice in the western hemisphere.

708 Another region of interest is the eastern part of Tombaugh Regio (the right lobe of the  
709 heart). Its surface is relatively bright and covered by N<sub>2</sub>-rich and CH<sub>4</sub>-rich frosts. Could it  
710 be a consequence of the retro-rotation of Pluto's atmosphere? The bright pitted uplands  
711 seen in the eastern part of Tombaugh Regio are thought to be a glacially-modified version  
712 of Bladed Terrain [Moore et al., 2018]. It is possible that they correspond to low-altitude  
713 Bladed Terrain deposits which became sufficiently bright at some point of Pluto's history  
714 to trigger N<sub>2</sub> ice condensation and accumulation on it, whereas high-altitude Bladed  
715 Terrain deposits remained N<sub>2</sub>-free because located at much higher altitude. Then, N<sub>2</sub> ice  
716 remained in east Tombaugh Regio as it is very stable at these latitudes [Bertrand et al.,  
717 2018, 2019]. Alternatively, gaseous CH<sub>4</sub> subliming from the CH<sub>4</sub>-rich Bladed Terrain  
718 would be transported westward by the retrograde winds and could quickly recondense in  
719 east Tombaugh Regio, thus forming bright ice deposits there. Albedo feedbacks would  
720 then be sufficient to trigger more CH<sub>4</sub> and N<sub>2</sub> condensation in this region [Bertrand et al.,  
721 2019; Earle et al., 2018]. However, we note that condensation of CH<sub>4</sub> west of the Bladed  
722 Terrain is not verified everywhere on Pluto. For instance, Bladed Terrain deposits are  
723 observed east of the Krun Macula region (south-east of Sputnik Planitia) but this region  
724 remains dark and is not covered by bright CH<sub>4</sub> frosts.

725 Finally, the ridges (“blades”) of the Bladed Terrain deposits display a dominant N-S  
726 orientation [Moore et al., 2018], which could also originate in part from this peculiar  
727 atmospheric circulation regime, although it may be a N-S-aligned sublimation texture  
728 due to equatorial location, as suggested by Moore et al. [2018]. In the future, we plan  
729 to further explore these ideas and investigate the processes leading to these longitudinal  
730 asymmetries and peculiar geological formations, by using high resolution long-term GCM  
731 simulations.

## 6. Conclusions

732 We explored Pluto’s atmosphere dynamics by using an improved version of the 3D LMD  
733 Global Climate Model of Pluto’s atmosphere, which now takes into account topographic  
734 datasets constructed for Pluto encounter hemisphere. We performed high resolution sim-  
735 ulations of Pluto’s climate for 2015, which are the result of 30-Earth-year simulations  
736 performed with the GCM at low resolution and 30-millions-year simulations performed  
737 with the 2D surface model (VTM). Based on the VTM results, we tested different possi-  
738 ble scenarios in the GCM, assuming an initial distribution of  $N_2$  ice only in the Sputnik  
739 Planitia basin or with additional mid-latitude  $N_2$  ice deposits.

740 In all simulation cases, we obtain an intense near-surface circulation within Sputnik  
741 Planitia, totally controlled by the  $N_2$  condensation-sublimation flow and the topography,  
742 and characterized in 2015 by an anti-clockwise spiral flow and a western boundary current.  
743 We explored if these near-surface winds could play a role in the formation of albedo and ice  
744 composition contrasts observed across Sputnik Planitia. We used the GCM to investigate  
745 different surface-atmosphere interactions involving the near-surface winds, such as the  
746 effect of the conductive heat flux from the atmosphere, the erosion of the ice, and the

747 transport of ice grains and dark materials. We find that the cumulative effect of these  
748 mechanisms could trigger significant contrasts in ice sublimation rate and color, and could  
749 explain the formation of the bright and dark plains in Sputnik Planitia.

750 We also find that the near-surface circulation adds up to the thermal gradient in the  
751 atmosphere to trigger a zonally-averaged meridional transport of  $N_2$  from the north-  
752 ern summer hemisphere to the southern winter hemisphere. By conservation of angular  
753 momentum, this leads unavoidably to a general circulation characterized by retrograde  
754 westward winds reaching up to  $10 \text{ m s}^{-1}$  above the equator, while meridional winds re-  
755 main relatively weak at all longitudes (less than  $1 \text{ m s}^{-1}$ ). This retro-rotation of Pluto's  
756 atmosphere is a unique circulation regime in the Solar system, except maybe on Triton,  
757 where pole-to-pole transport of  $N_2$  could also lead to a similar regime. We find that the  
758 retro-rotation is maintained during most of Pluto's year. It could be responsible for many  
759 longitudinal asymmetries and geological features observed on Pluto's surface, such as the  
760 depletion of Bladed Terrains at eastern longitudes and the formation of bright pits in  
761 eastern Tombaugh regio, although this remains to be explored. Our work confirms that  
762 despite a frozen surface and a tenuous atmosphere, Pluto's climate is remarkably active.

763 **Acknowledgments.** We thank John Wilson, Bob Haberle and Melinda Kahre for in-  
764 sightful discussions and comparisons between Mars and Pluto. We thank the NASA  
765 New Horizons team for their excellent work on a fantastic mission and their interest in  
766 this research. We acknowledge the Centre National dEtudes Spatiales (CNES) for its  
767 financial support through its "Système Solaire" program. T. B. was supported for this re-  
768 search by an appointment to the National Aeronautics and Space Administration (NASA)  
769 Post-doctoral Program at the Ames Research Center administered by Universities Space

770 Research Association (USRA) through a contract with NASA. Electronic output from all  
771 model simulations will be made available to the public through the NASA Advanced Su-  
772 percomputing (NAS) data portal (<https://data.nas.nasa.gov/>), which is housed at NASA  
773 Ames Research Center.

**References**

- 774 D. L. T. Anderson. The Low-Level Jet as a Western Boundary Current. *Monthly Weather*  
775 *Review*, 104:907, 1976. doi: 10.1175/1520-0493(1976)104(0907:TLLJAA)2.0.CO;2.
- 776 T. Appéré, B. Schmitt, Y. Langevin, S. Douté, A. Pommerol, F. Forget, A. Spiga,  
777 B. Gondet, and J.-P. Bibring. Winter and spring evolution of northern seasonal deposits  
778 on Mars from OMEGA on Mars Express. *Journal of Geophysical Research (Planets)*,  
779 116:E05001, May 2011. doi: 10.1029/2010JE003762.
- 780 T. Bertrand and F. Forget. Observed glacier and volatile distribution on Pluto from atmo-  
781 spheretopography processes. *Nature*, 987, December 2016. doi: 10.1038/nature19337.
- 782 T. Bertrand and F. Forget. 3D modeling of organic haze in Pluto’s atmosphere. *Icarus*,  
783 287:72–86, May 2017. doi: 10.1016/j.icarus.2017.01.016.
- 784 T. Bertrand, F. Forget, O. M. Umurhan, W. M. Grundy, B. Schmitt, S. Protopapa, A. M.  
785 Zangari, O. L. White, P. M. Schenk, K. N. Singer, A. Stern, H. A. Weaver, L. A. Young,  
786 K. Ennico, and C. B. Olkin. The nitrogen cycles on Pluto over seasonal and astronomical  
787 timescales. *Icarus*, 309:277–296, July 2018. doi: 10.1016/j.icarus.2018.03.012.
- 788 T. Bertrand, F. Forget, O. M. Umurhan, J. M. Moore, L. A. Young, S. Protopapa, W. M.  
789 Grundy, B. Schmitt, R. D. Dhingra, and R. P. Binzel. The CH<sub>4</sub> cycles on Pluto over  
790 seasonal and astronomical timescales. *Icarus*, 329:148–165, Sep 2019. doi: 10.1016/j.  
791 icarus.2019.02.007.
- 792 R. P. Binzel, A. M. Earle, M. W. Buie, L. A. Young, S. A. Stern, C. B. Olkin, K. Ennico,  
793 J. M. Moore, W. Grundy, H. A. Weaver, C. M. Lisse, and T. R. Lauer. Climate zones  
794 on Pluto and Charon. *Icarus*, 287:30–36, May 2017. doi: 10.1016/j.icarus.2016.07.023.

795 B. J. Buratti, J. D. Hofgartner, M. D. Hicks, H. A. Weaver, S. A. Stern, T. Momary,  
796 J. A. Mosher, R. A. Beyer, A. J. Verbiscer, A. M. Zangari, L. A. Young, C. M. Lisse,  
797 K. Singer, A. Cheng, W. Grundy, K. Ennico, and C. B. Olkin. Global albedos of Pluto  
798 and Charon from LORRI New Horizons observations. *Icarus*, 287:207–217, May 2017.  
799 doi: 10.1016/j.icarus.2016.11.012.

800 A. M. Earle, R. P. Binzel, L. A. Young, S. A. Stern, K. Ennico, W. Grundy, C. B.  
801 Olkin, H. A. Weaver, and New Horizons Surface Composition Theme. Albedo matters:  
802 Understanding runaway albedo variations on Pluto. *Icarus*, 303:1–9, March 2018. doi:  
803 10.1016/j.icarus.2017.12.015.

804 J. L. Elliot, A. Ates, B. A. Babcock, A. S. Bosh, M. W. Buie, K. B. Clancy, E. W. Dunham,  
805 S. S. Eikenberry, D. T. Hall, S. D. Kern, S. K. Leggett, S. E. Levine, D.-S. Moon, C. B.  
806 Olkin, D. J. Osip, J. M. Pasachoff, B. E. Penprase, M. J. Person, S. Qu, J. T. Rayner,  
807 L. C. Roberts, C. V. Salyk, S. P. Souza, R. C. Stone, B. W. Taylor, D. J. Tholen, J. E.  
808 Thomas-Osip, D. R. Ticehurst, and L. H. Wasserman. The recent expansion of Pluto’s  
809 atmosphere. *Nature*, 424:165–168, July 2003. doi: 10.1038/nature01762.

810 F. Forget, T. Bertrand, M. Vangvichith, J. Leconte, E. Millour, and E. Lellouch. A  
811 post-new horizons global climate model of Pluto including the N<sub>2</sub>, CH<sub>4</sub> and CO cycles.  
812 *Icarus*, 287:54–71, May 2017. doi: 10.1016/j.icarus.2016.11.038.

813 P. E. Geissler. Three decades of Martian surface changes. *Journal of Geophysical Research*  
814 (*Planets*), 110:E02001, February 2005. doi: 10.1029/2004JE002345.

815 R. Greeley, A. Skyeck, and J. B. Pollack. Martian aeolian features and deposits -  
816 Comparisons with general circulation model results. *J. Geophys. Res.*, , 98:3183–3196,  
817 February 1993. doi: 10.1029/92JE02580.

818 W. M. Grundy, R. P. Binzel, B. J. Buratti, J. C. Cook, D. P. Cruikshank, C. M. Dalle  
819 Ore, A. M. Earle, K. Ennico, C. J. A. Howett, A. W. Lunsford, C. B. Olkin, A. H.  
820 Parker, S. Philippe, S. Protopapa, E. Quirico, D. C. Reuter, B. Schmitt, K. N. Singer,  
821 A. J. Verbiscer, R. A. Beyer, M. W. Buie, A. F. Cheng, D. E. Jennings, I. R. Linscott,  
822 J. W. Parker, P. M. Schenk, J. R. Spencer, J. A. Stansberry, S. A. Stern, H. B. Throop,  
823 C. C. C. Tsang, H. A. Weaver, G. E. Weigle, and L. A. Young. Surface compositions  
824 across Pluto and Charon. *Science*, 351:aad9189, March 2016. doi: 10.1126/science.  
825 aad9189.

826 W. M. Grundy, T. Bertrand, R. P. Binzel, M. W. Buie, B. J. Buratti, A. F. Cheng,  
827 J. C. Cook, D. P. Cruikshank, S. L. Devins, C. M. Dalle Ore, A. M. Earle, K. Ennico,  
828 F. Forget, P. Gao, G. R. Gladstone, C. J. A. Howett, D. E. Jennings, J. A. Kammer,  
829 T. R. Lauer, I. R. Linscott, C. M. Lisse, A. W. Lunsford, W. B. McKinnon, C. B. Olkin,  
830 A. H. Parker, S. Protopapa, E. Quirico, D. C. Reuter, B. Schmitt, K. N. Singer, J. A.  
831 Spencer, S. A. Stern, D. F. Strobel, M. E. Summers, H. A. Weaver, G. E. Weigle, M. L.  
832 Wong, E. F. Young, L. A. Young, and X. Zhang. Pluto’s haze as a surface material.  
833 *Icarus*, 314:232–245, November 2018. doi: 10.1016/j.icarus.2018.05.019.

834 C. J. Hansen and D. A. Paige. Seasonal Nitrogen Cycles on Pluto. *Icarus*, 120:247–265,  
835 April 1996. doi: 10.1006/icar.1996.0049.

836 D. P. Hinson, I. R. Linscott, L. A. Young, G. L. Tyler, S. A. Stern, R. A. Beyer, M. K.  
837 Bird, K. Ennico, G. R. Gladstone, C. B. Olkin, M. Pätzold, P. M. Schenk, D. F. Strobel,  
838 M. E. Summers, H. A. Weaver, and W. W. Woods. Radio occultation measurements  
839 of Pluto’s neutral atmosphere with New Horizons. *Icarus*, 290:96–111, July 2017. doi:  
840 10.1016/j.icarus.2017.02.031.

- 841 A. D. Howard, J. M. Moore, O. M. Umurhan, O. L. White, R. S. Anderson, W. B.  
842 McKinnon, J. R. Spencer, P. M. Schenk, R. A. Beyer, S. A. Stern, K. Ennico, C. B.  
843 Olkin, H. A. Weaver, and L. A. Young. Present and past glaciation on Pluto. *Icarus*,  
844 287:287–300, May 2017. doi: 10.1016/j.icarus.2016.07.006.
- 845 M. M. Joshi, S. R. Lewis, P. L. Read, and D. C. Catling. Western boundary currents in  
846 the atmosphere of Mars. *Nature*, 367:548–552, February 1994. doi: 10.1038/367548a0.
- 847 M. M. Joshi, S. R. Lewis, P. L. Read, and D. C. Catling. Western boundary currents in the  
848 Martian atmosphere: Numerical simulations and observational evidence. *J. Geophys.*  
849 *Res.*, , 100:5485–5500, March 1995. doi: 10.1029/94JE02716.
- 850 W. B. McKinnon, F. Nimmo, T. Wong, P. M. Schenk, O. L. White, J. H. Roberts, J. M.  
851 Moore, J. R. Spencer, A. D. Howard, O. M. Umurhan, S. A. Stern, H. A. Weaver,  
852 C. B. Olkin, L. A. Young, K. E. Smith, R. Beyer, M. Buie, B. Buratti, A. Cheng,  
853 D. Cruikshank, C. Dalle Ore, R. Gladstone, W. Grundy, T. Lauer, I. Linscott, J. Parker,  
854 S. Porter, H. Reitsema, D. Reuter, S. Robbins, M. Showalter, K. Singer, D. Strobel,  
855 M. Summers, L. Tyler, M. Banks, O. Barnouin, V. Bray, B. Carcich, A. Chaikin,  
856 C. Chavez, C. Conrad, D. Hamilton, C. Howett, J. Hofgartner, J. Kammer, C. Lisse,  
857 A. Marcotte, A. Parker, K. Retherford, M. Saina, K. Runyon, E. Schindhelm, J. Stans-  
858 berry, A. Steffl, T. Stryk, H. Throop, C. Tsang, A. Verbiscer, H. Winters, A. Zan-  
859 gari, and G. a. I. T. T. New Horizons Geology. Convection in a volatile nitrogen-  
860 ice-rich layer drives Pluto’s geological vigour. *Nature*, 534:82–85, June 2016. doi:  
861 10.1038/nature18289.
- 862 E. Meza, B. Sicardy, M. Assafin, J. L. Ortiz, T. Bertrand, E. Lellouch, J. Desmars, F. For-  
863 get, D. Bérard, A. Doressoundiram, J. Lecacheux, J. Marques Oliveira, F. Roques,

864 T. Widemann, F. Colas, F. Vachier, S. Renner, R. Leiva, F. Braga-Ribas, G. Benedetti-  
865 Rossi, J. I. B. Camargo, A. Dias-Oliveira, B. Morgado, A. R. Gomes-Júnior, R. Vieira-  
866 Martins, R. Behrend, A. Castro Tirado, R. Duffard, N. Morales, P. Santos-Sanz,  
867 M. Jelínek, R. Cunniffe, R. Querel, M. Harnisch, R. Jansen, A. Pennell, S. Todd, V. D.  
868 Ivanov, C. Opitom, M. Gillon, E. Jehin, J. Manfroid, J. Pollock, D. E. Reichart, J. B.  
869 Haislip, K. M. Ivarsen, A. P. LaCluyze, A. Maury, R. Gil-Hutton, V. Dhillon, S. Little-  
870 fair, T. Marsh, C. Veillet, K. L. Bath, W. Beisker, H. J. Bode, M. Kretlow, D. Herald,  
871 D. Gault, S. Kerr, H. Pavlov, O. Faragó, O. Klös, E. Frappa, M. Lavayssière, A. A.  
872 Cole, A. B. Giles, J. G. Greenhill, K. M. Hill, M. W. Buie, C. B. Olkin, E. F. Young,  
873 L. A. Young, L. H. Wasserman, M. Devogèle, R. G. French, F. B. Bianco, F. Marchis,  
874 N. Brosch, S. Kaspi, D. Polishook, I. Manulis, M. Ait Moulay Larbi, Z. Benkhaldoun,  
875 A. Daassou, Y. El Azhari, Y. Moulane, J. Broughton, J. Milner, T. Dobosz, G. Bolt,  
876 B. Lade, A. Gilmore, P. Kilmartin, W. H. Allen, P. B. Graham, B. Loader, G. McKay,  
877 J. Talbot, S. Parker, L. Abe, Ph. Bendjoya, J. P. Rivet, D. Vernet, L. Di Fabrizio,  
878 V. Lorenzi, A. Magazzú, E. Molinari, K. Gazeas, L. Tzouganatos, A. Carbognani,  
879 G. Bonnoli, A. Marchini, G. Leto, R. Zanmar Sanchez, L. Mancini, B. Kattentidt,  
880 M. Dohrmann, K. Guhl, W. Rothe, K. Walzel, G. Wortmann, A. Eberle, D. Hampf,  
881 J. Ohlert, G. Krannich, G. Murawsky, B. Gährken, D. Gloistein, S. Alonso, A. Román,  
882 J. E. Communal, F. Jabet, S. deVisscher, J. Sérot, T. Janik, Z. Moravec, P. Machado,  
883 A. Selva, C. Perelló, J. Rovira, M. Conti, R. Papini, F. Salvaggio, A. Noschese,  
884 V. Tsamis, K. Tigani, P. Barroy, M. Irzyk, D. Neel, J. P. Godard, D. Lanoiselée, P. So-  
885 gorb, D. Vérilhac, M. Bretton, F. Signoret, F. Ciabattari, R. Naves, M. Boutet, J. De  
886 Queiroz, P. Lindner, K. Lindner, P. Enskonatus, G. Dangl, T. Tordai, H. Eichler, J. Hat-

- 887 tenbach, C. Peterson, L. A. Molnar, and R. R. Howell. Lower atmosphere and pressure  
888 evolution on Pluto from ground-based stellar occultations, 1988-2016. *Astronomy and*  
889 *Astrophysics*, 625:A42, May 2019. doi: 10.1051/0004-6361/201834281.
- 890 J. M. Moore, A. D. Howard, O. M. Umurhan, O. L. White, P. M. Schenk, R. A. Beyer,  
891 W. B. McKinnon, J. R. Spencer, K. N. Singer, W. M. Grundy, A. M. Earle, B. Schmitt,  
892 S. Protopapa, F. Nimmo, D. P. Cruikshank, D. P. Hinson, L. A. Young, S. A. Stern,  
893 H. A. Weaver, C. B. Olkin, K. Ennico, G. Collins, T. Bertrand, F. Forget, F. Scipi-  
894 oni, and New Horizons Science Team. Bladed Terrain on Pluto: Possible origins and  
895 evolution. *Icarus*, 300:129–144, January 2018. doi: 10.1016/j.icarus.2017.08.031.
- 896 J. E. Moores, C. L. Smith, A. D. Toigo, and S. D. Guzewich. Penitentes as the origin of  
897 the bladed terrain of Tartarus Dorsa on Pluto. *Nature*, 541:188–190, January 2017. doi:  
898 10.1038/nature20779.
- 899 C. B. Olkin, J. R. Spencer, W. M. Grundy, A. H. Parker, R. A. Beyer, P. M. Schenk,  
900 C. J. A. Howett, S. A. Stern, D. C. Reuter, H. A. Weaver, L. A. Young, K. Ennico,  
901 R. P. Binzel, M. W. Buie, J. C. Cook, D. P. Cruikshank, C. M. Dalle Ore, A. M. Earle,  
902 D. E. Jennings, K. N. Singer, I. E. Linscott, A. W. Lunsford, S. Protopapa, B. Schmitt,  
903 E. Weigle, and the New Horizons Science Team. The Global Color of Pluto from New  
904 Horizons. *Astron. J.*, , 154:258, December 2017. doi: 10.3847/1538-3881/aa965b.
- 905 M. J. Person, J. L. Elliot, A. A. S. Gulbis, C. A. Zuluaga, B. A. Babcock, A. J. McKay,  
906 J. M. Pasachoff, S. P. Souza, W. B. Hubbard, C. A. Kulesa, D. W. McCarthy, S. D.  
907 Benecchi, S. E. Levine, A. S. Bosh, E. V. Ryan, W. H. Ryan, A. Meyer, J. Wolf, and  
908 J. Hill. Waves in Pluto’s Upper Atmosphere. *Astrophys. J.*, 136:1510–1518, October  
909 2008. doi: 10.1088/0004-6256/136/4/1510.

- 910 S. Protopapa, W. M. Grundy, D. C. Reuter, D. P. Hamilton, C. M. Dalle Ore, J. C.  
911 Cook, D. P. Cruikshank, B. Schmitt, S. Philippe, E. Quirico, R. P. Binzel, A. M. Earle,  
912 K. Ennico, C. J. A. Howett, A. W. Lunsford, C. B. Olkin, A. Parker, K. N. Singer,  
913 A. Stern, A. J. Verbiscer, H. A. Weaver, and L. A. Young. Pluto's global surface  
914 composition through pixel-by-pixel Hapke modeling of New Horizons Ralph/LEISA  
915 data. *Icarus*, 287:218–228, May 2017. doi: 10.1016/j.icarus.2016.11.028.
- 916 P. M. Schenk, R. A. Beyer, W. B. McKinnon, J. M. Moore, J. R. Spencer, O. L. White,  
917 K. Singer, F. Nimmo, C. Thomason, T. R. Lauer, S. Robbins, O. M. Umurhan, W. M.  
918 Grundy, S. A. Stern, H. A. Weaver, L. A. Young, K. E. Smith, C. Olkin, New Hori-  
919 zons Geology, and Geophysics Investigation Team. Basins, fractures and volcanoes:  
920 Global cartography and topography of Pluto from New Horizons. *Icarus*, 314:400–433,  
921 November 2018. doi: 10.1016/j.icarus.2018.06.008.
- 922 B. Schmitt, S. Philippe, W. M. Grundy, D. C. Reuter, R. Cote, E. Quirico, S. Protopapa,  
923 L. A. Young, R. P. Binzel, J. C. Cook, D. P. Cruikshank, C. M. Dalle Ore, A. M. Earle,  
924 K. Ennico, C. J. A. Howett, D. E. Jennings, I. R. Linscott, A. W. Lunsford, C. B. Olkin,  
925 A. H. Parker, J. W. Parker, K. N. Singer, J. R. Spencer, J. A. Stansberry, S. A. Stern,  
926 C. C. C. Tsang, A. J. Verbiscer, and H. A. Weaver. Physical state and distribution  
927 of materials at the surface of Pluto from New Horizons LEISA imaging spectrometer.  
928 *Icarus*, 287:229–260, May 2017. doi: 10.1016/j.icarus.2016.12.025.
- 929 A. Spiga, F. Forget, J.-B. Madeleine, L. Montabone, S. R. Lewis, and E. Millour. The  
930 impact of martian mesoscale winds on surface temperature and on the determination  
931 of thermal inertia. *Icarus*, 212:504–519, April 2011. doi: 10.1016/j.icarus.2011.02.001.

932 J. A. Stansberry, J. I. Lunine, and M. G. Tomasko. Upper limits on possible photochemical  
933 hazes on Pluto. *Geophys. Res. Lett.*, 16:1221–1224, November 1989. doi: 10.1029/  
934 GL016i011p01221.

935 S. A. Stern, F. Bagenal, K. Ennico, G. R. Gladstone, W. M. Grundy, W. B. McKinnon,  
936 J. M. Moore, C. B. Olkin, J. R. Spencer, H. A. Weaver, L. A. Young, T. Andert, J. An-  
937 drews, M. Banks, B. Bauer, J. Bauman, O. S. Barnouin, P. Bedini, K. Beisser, R. A.  
938 Beyer, S. Bhaskaran, R. P. Binzel, E. Birath, M. Bird, D. J. Bogan, A. Bowman, V. J.  
939 Bray, M. Brozovic, C. Bryan, M. R. Buckley, M. W. Buie, B. J. Buratti, S. S. Bush-  
940 man, A. Calloway, B. Carcich, A. F. Cheng, S. Conard, C. A. Conrad, J. C. Cook, D. P.  
941 Cruikshank, O. S. Custodio, C. M. Dalle Ore, C. Deboy, Z. J. B. Dischner, P. Dumont,  
942 A. M. Earle, H. A. Elliott, J. Ercol, C. M. Ernst, T. Finley, S. H. Flanigan, G. Foun-  
943 tain, M. J. Freeze, T. Greathouse, J. L. Green, Y. Guo, M. Hahn, D. P. Hamilton, S. A.  
944 Hamilton, J. Hanley, A. Harch, H. M. Hart, C. B. Hersman, A. Hill, M. E. Hill, D. P.  
945 Hinson, M. E. Holdridge, M. Horanyi, A. D. Howard, C. J. A. Howett, C. Jackman,  
946 R. A. Jacobson, D. E. Jennings, J. A. Kammer, H. K. Kang, D. E. Kaufmann, P. Koll-  
947 mann, S. M. Krimigis, D. Kusnierkiewicz, T. R. Lauer, J. E. Lee, K. L. Lindstrom, I. R.  
948 Linscott, C. M. Lisse, A. W. Lunsford, V. A. Mallder, N. Martin, D. J. McComas, R. L.  
949 McNutt, D. Mehoke, T. Mehoke, E. D. Melin, M. Mutchler, D. Nelson, F. Nimmo,  
950 J. I. Nunez, A. Ocampo, W. M. Owen, M. Paetzold, B. Page, A. H. Parker, J. W.  
951 Parker, F. Pelletier, J. Peterson, N. Pinkine, M. Piquette, S. B. Porter, S. Protopapa,  
952 J. Redfern, H. J. Reitsema, D. C. Reuter, J. H. Roberts, S. J. Robbins, G. Rogers,  
953 D. Rose, K. Runyon, K. D. Retherford, M. G. Ryschkewitsch, P. Schenk, E. Schind-  
954 helm, B. Sepan, M. R. Showalter, K. N. Singer, M. Soluri, D. Stanbridge, A. J. Steffl,

- 955 D. F. Strobel, T. Stryk, M. E. Summers, J. R. Szalay, M. Tapley, A. Taylor, H. Taylor,  
956 H. B. Throop, C. C. C. Tsang, G. L. Tyler, O. M. Umurhan, A. J. Verbiscer, M. H.  
957 Versteeg, M. Vincent, R. Webbert, S. Weidner, G. E. Weigle, O. L. White, K. Whit-  
958 tenburg, B. G. Williams, K. Williams, S. Williams, W. W. Woods, A. M. Zangari, and  
959 E. Zirnstein. The Pluto system: Initial results from its exploration by New Horizons.  
960 *Science*, 350:aad1815, October 2015. doi: 10.1126/science.aad1815.
- 961 D. F. Strobel, X. Zhu, M. E. Summers, and M. H. Stevens. On the Vertical Thermal  
962 Structure of Pluto’s Atmosphere. *Icarus*, 120:266–289, April 1996. doi: 10.1006/icar.  
963 1996.0050.
- 964 M. W. Telfer, E. J. R. Parteli, J. Radebaugh, R. A. Beyer, T. Bertrand, F. Forget,  
965 F. Nimmo, W. M. Grundy, J. M. Moore, S. A. Stern, J. Spencer, T. R. Lauer, A. M.  
966 Earle, R. P. Binzel, H. A. Weaver, C. B. Olkin, L. A. Young, K. Ennico, K. Runyon, and  
967 aff12. Dunes on Pluto. *Science*, 360:992–997, June 2018. doi: 10.1126/science.aao2975.
- 968 P. Thomas, J. Veverka, S. Lee, and A. Bloom. Classification of wind streaks on Mars.  
969 *Icarus*, 45:124–153, January 1981. doi: 10.1016/0019-1035(81)90010-5.
- 970 A. D. Toigo, P. J. Gierasch, B. Sicardy, and E. Lellouch. Thermal tides on Pluto. *Icarus*,  
971 208:402–411, July 2010. doi: 10.1016/j.icarus.2010.01.027.
- 972 A. D. Toigo, R. G. French, P. J. Gierasch, S. D. Guzewich, X. Zhu, and M. I. Richardson.  
973 General circulation models of the dynamics of Pluto’s volatile transport on the eve of  
974 the New Horizons encounter. *Icarus*, 254:306–323, July 2015. doi: 10.1016/j.icarus.  
975 2015.03.034.
- 976 O. L. White, J. M. Moore, W. B. McKinnon, J. R. Spencer, A. D. Howard, P. M. Schenk,  
977 R. A. Beyer, F. Nimmo, K. N. Singer, O. M. Umurhan, S. A. Stern, K. Ennico, C. B.

978 Olkin, H. A. Weaver, L. A. Young, A. F. Cheng, T. Bertrand, R. P. Binzel, A. M.  
979 Earle, W. M. Grundy, T. R. Lauer, S. Protopapa, S. J. Robbins, and B. Schmitt.  
980 Geological mapping of Sputnik Planitia on Pluto. *Icarus*, 287:261–286, May 2017. doi:  
981 10.1016/j.icarus.2017.01.011.

982 L. A. Young. Pluto’s Seasons: New Predictions for New Horizons. *Astrophys. J.l*, 766:  
983 L22, April 2013. doi: 10.1088/2041-8205/766/2/L22.

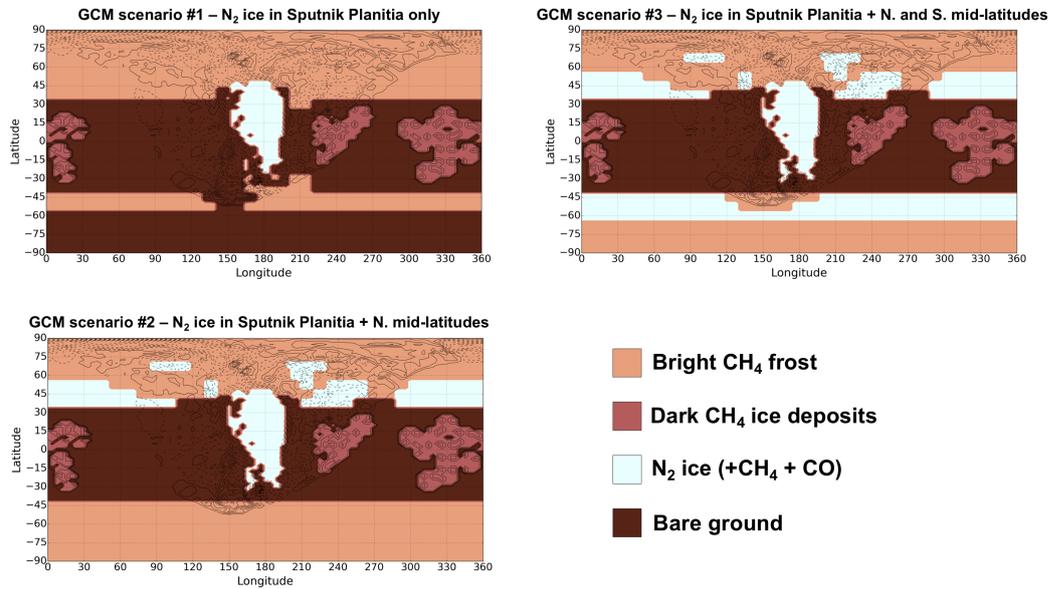


**Figure 1.** Map of initial surface ice distribution for the three GCM simulations. Albedos of each ice have been set so that the surface pressure and the atmospheric mixing ratio of CH<sub>4</sub> match the observations made by New Horizons in 2015. #1:  $A_{N_2}=0.7, A_{CH_4}=0.65$ . #2:  $A_{N_2}=0.74, A_{CH_4}=0.68$ . #3:  $A_{N_2}=0.67, A_{CH_4}=0.7$ .

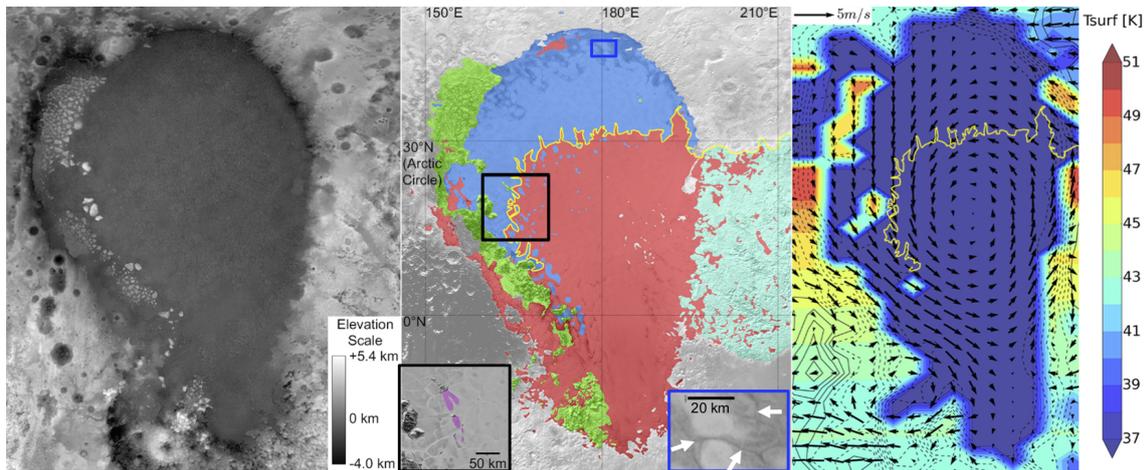


**Figure 2.** (A) Stereo digital elevation model (DEM) of Sputnik Planitia and surrounding terrain [Schenk et al., 2018]. (B) Simplified version of the geological map of White et al. [2017] depicting bright  $N_2$  ice plains (red), dark  $N_2$  ice plains (blue), mountains and hills lining the western rim of Sputnik Planitia (green), and bright pitted uplands of east Tombaugh Regio (cyan). Yellow line maps the continuous boundary between the bright and dark plains, as well as the northern boundary of the bright pitted uplands. Black box indicates the location of features in Sputnik Planitia interpreted as wind streaks, as mapped in purple in the inset (adapted from Stern et al. [2015]; Telfer et al. [2018]). Blue box and white arrows indicates the location of dark troughs, possibly filled with dark materials White et al. [2017]. (C) Map of diurnal mean horizontal winds in Sputnik Planitia obtained with the model for July 2015 at 1000 m above the surface. Yellow line replicates the bright/dark boundary in (B).

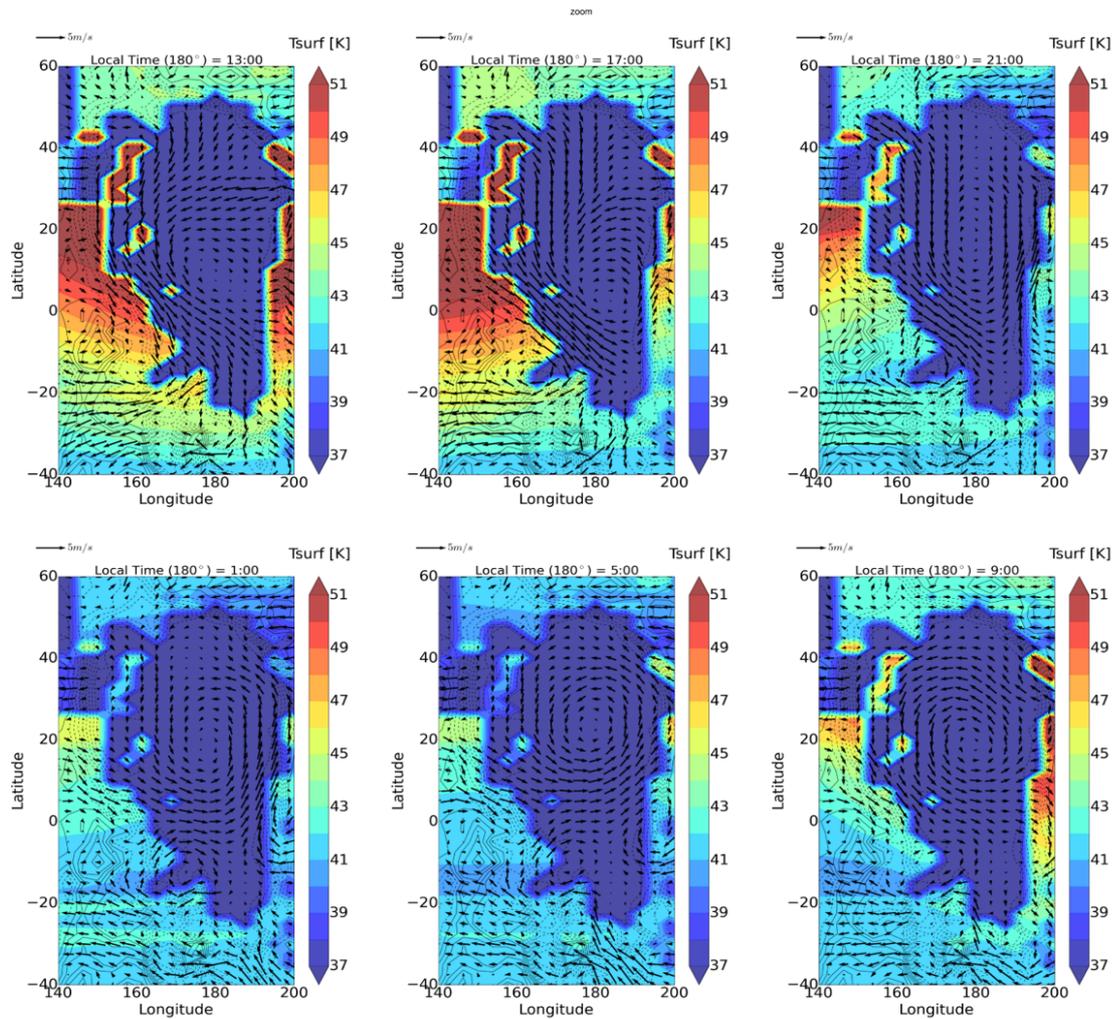


**Figure 3.** The beating of Pluto’s heart: diurnal variations of horizontal winds in Sputnik Planitia obtained with the GCM for July 2015 at 1000 m above the surface (for Scenario #1), showing western and eastern boundary currents. Winds are strongest during afternoon and weakest during morning. The anti-clockwise atmospheric spiral circulates continuously. Similar results are obtained for Scenario #2 and #3 (not shown)

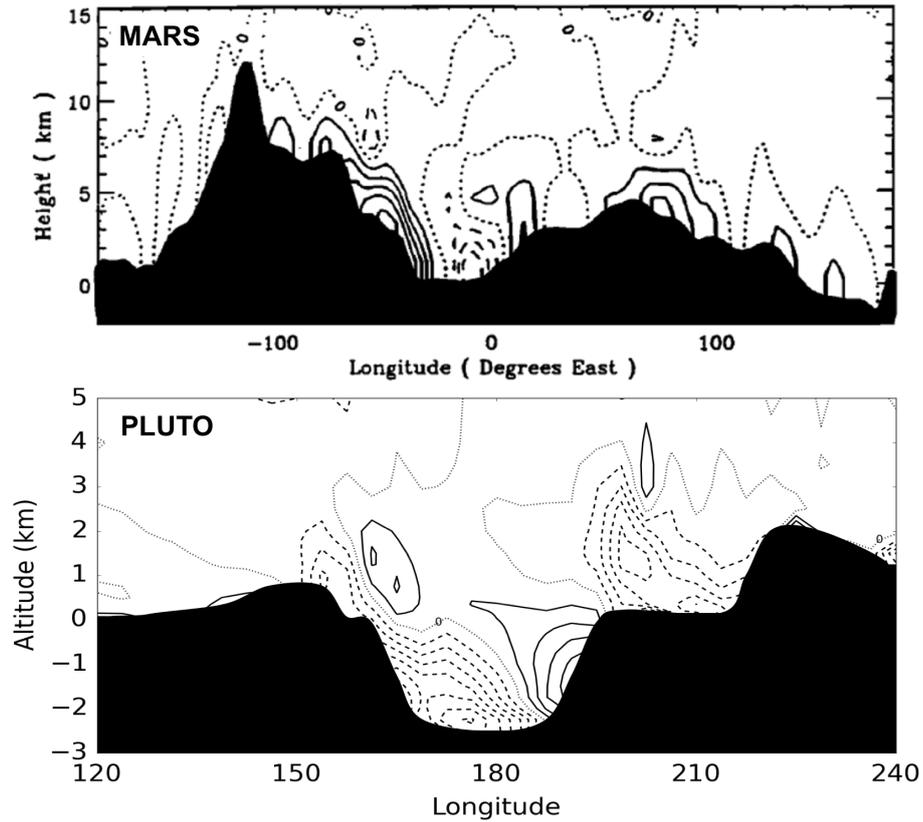


**Figure 4.** Cross-sections of the diurnal-averaged meridional wind (A) from Mars GCM simulations by Joshi et al. [1994], at the equator for northern summer solstice conditions (clockwise current) (B) from our Pluto GCM simulations, at the equator in the encounter hemisphere, in 2015 (northern spring, anti-clockwise current). The topographic profiles are shown in black. Contour intervals are  $5 \text{ m s}^{-1}$  for Mars and  $0.4 \text{ m s}^{-1}$  for Pluto, with the zero-contour dotted and negative contours dashed.

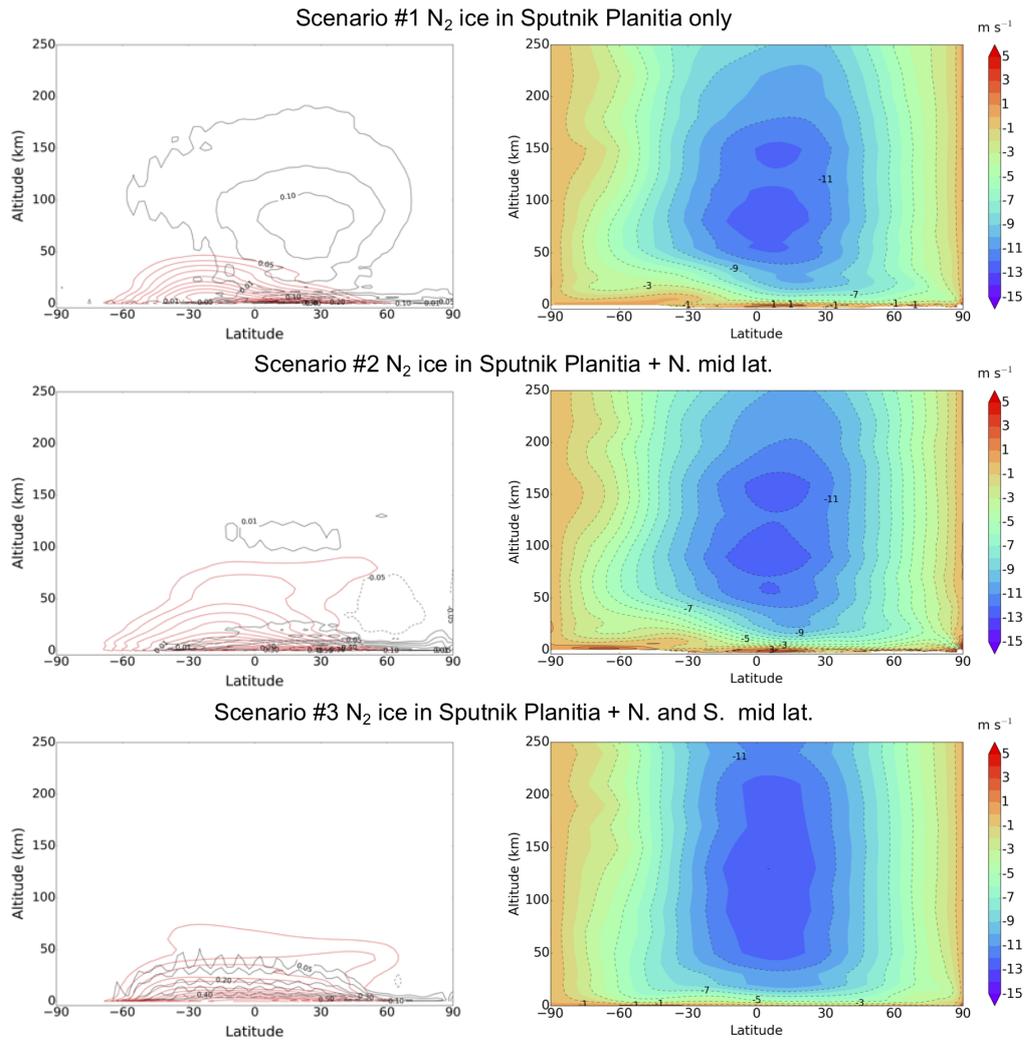


**Figure 5.** Left column: zonally averaged mass stream functions in units of  $10^6 \text{ kg s}^{-1}$  (black contour) and angular momentum (red contoured) as obtained for July 2015 in the three GCM simulations explored in this paper. Solid lines denote counterclockwise circulation. Small values of the stream function and angular momentum are not contoured. Note that the streamlines near the surface are not shown as the near-surface winds are strongly and locally impacted by the topography (with mostly katabatic downslope winds) and sublimation-condensation flows. Right column: zonally averaged zonal winds (in  $\text{m s}^{-1}$ ) obtained in the GCM simulations, showing that the general circulation is dominated by retrograde winds in all three cases.

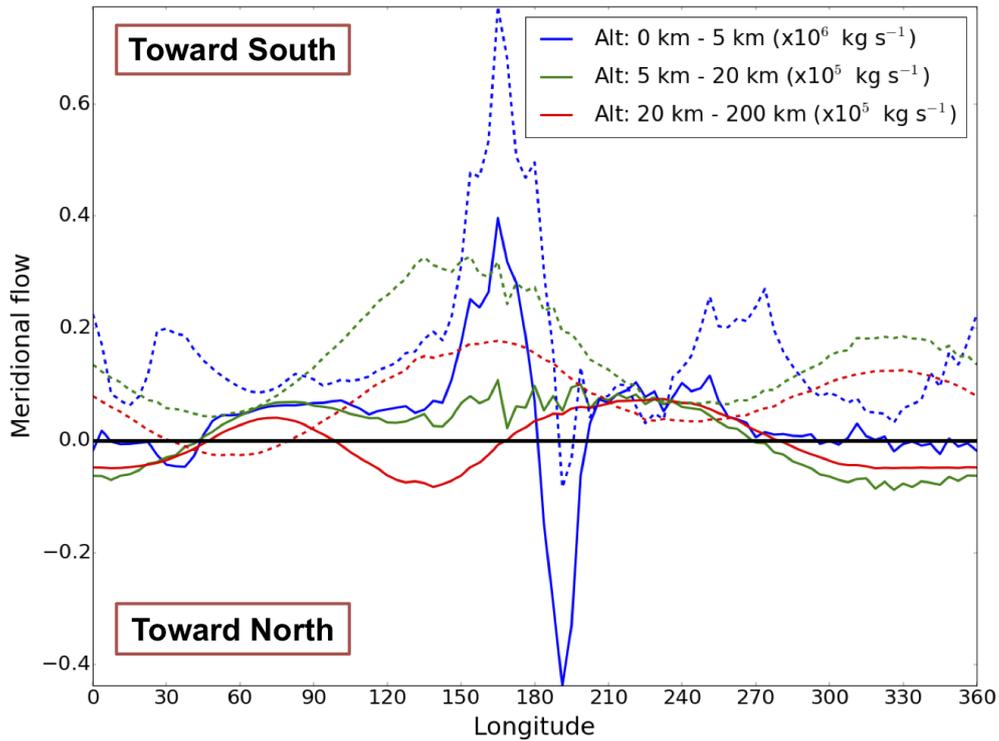


**Figure 6.** Southward meridional air mass flow averaged between  $45^{\circ}\text{S}$ - $45^{\circ}\text{N}$  for different ranges of altitudes, obtained for GCM scenarios #1 (solid lines) and #3 (dotted lines).

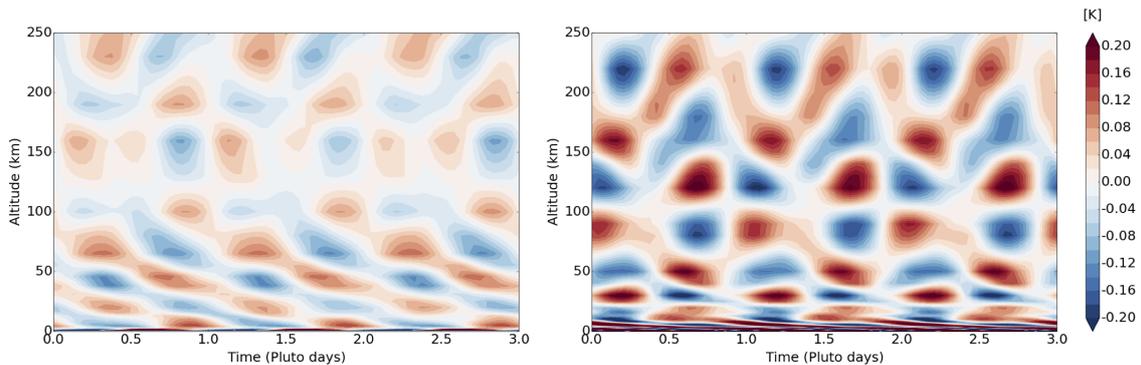


**Figure 7.** Temperature anomaly (difference between instantaneous value and diurnal average) showing diurnal thermal tides at  $0^{\circ}\text{E}$ - $0^{\circ}\text{N}$  in simulations #1 (left) and #3 (right) obtained with the GCM in July 2015.

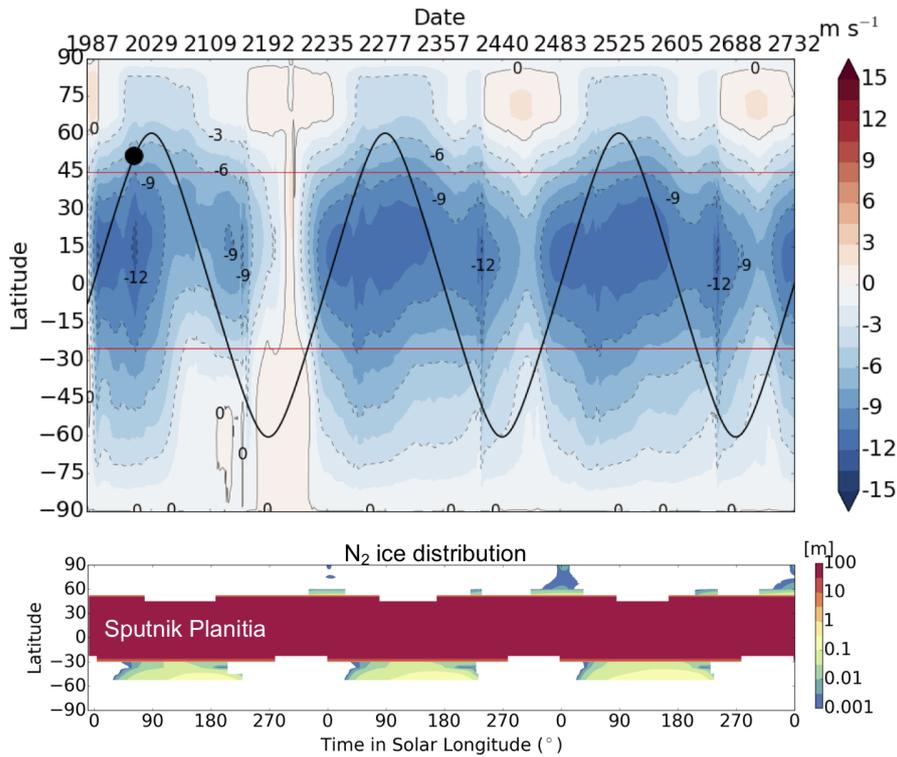


**Figure 8.** Annual evolution of Pluto’s general atmospheric circulation obtained with the GCM. (Top) Zonal mean zonal winds at 20 km above local surface obtained with the  $11.25^\circ \times 7.5^\circ$  GCM simulations over one Pluto year. The black solid line indicates the latitude of the subsolar point and its position in 2015 is shown by the black circle. The red horizontal solid lines indicate the bounding latitudes of Sputnik Planitia. The general circulation is dominated by a retro-rotation during most of the year. (Bottom) Zonal mean N<sub>2</sub> ice distribution (Sputnik Planitia is a permanent equatorial km-thick N<sub>2</sub> ice sheet).

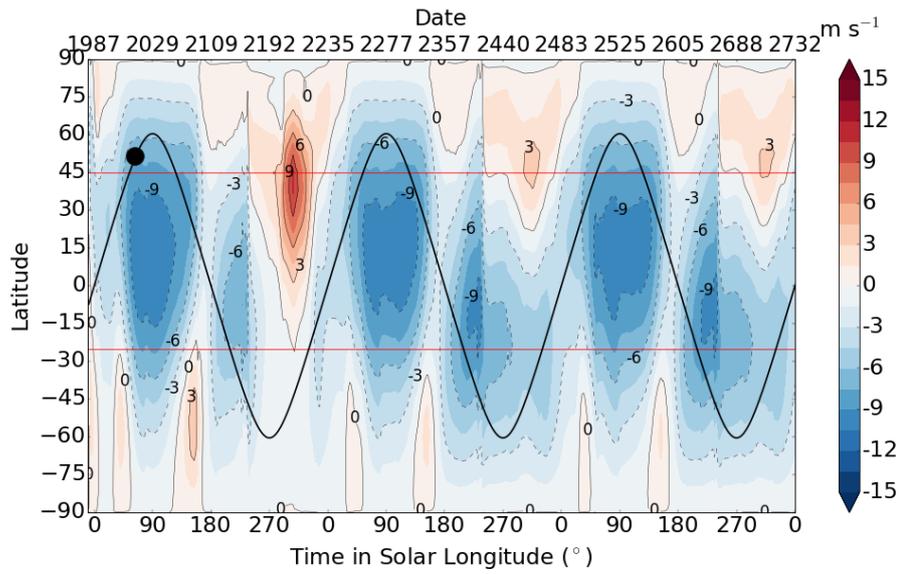


**Figure 9.** Same as Figure 8, but for an altitude of 100 km above the local surface

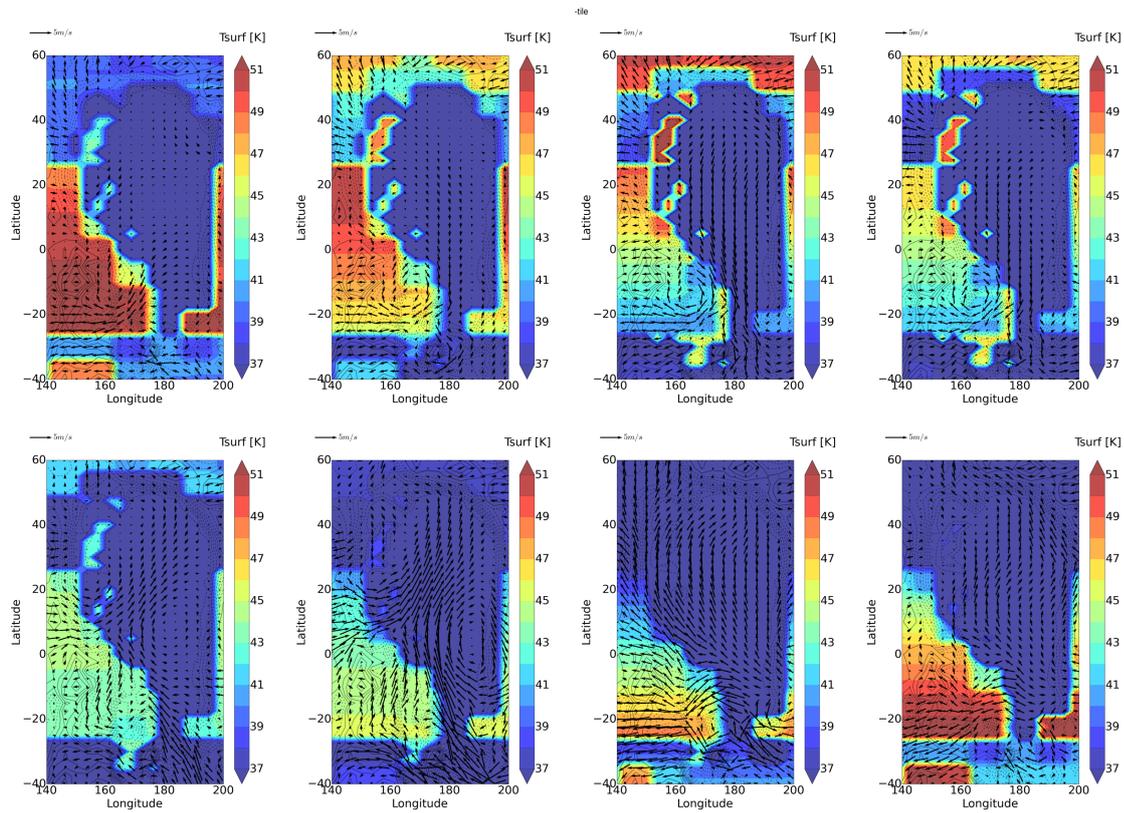


**Figure 10.** Diurnal mean horizontal winds in Sputnik Planitia obtained with the model at 1000 m above the surface, for  $L_s = 0^\circ, 45^\circ, 90^\circ, 135^\circ$  (northern spring and summer, top) and  $L_s = 180^\circ, 225^\circ, 270^\circ$  and  $315^\circ$  (northern fall and winter, bottom).

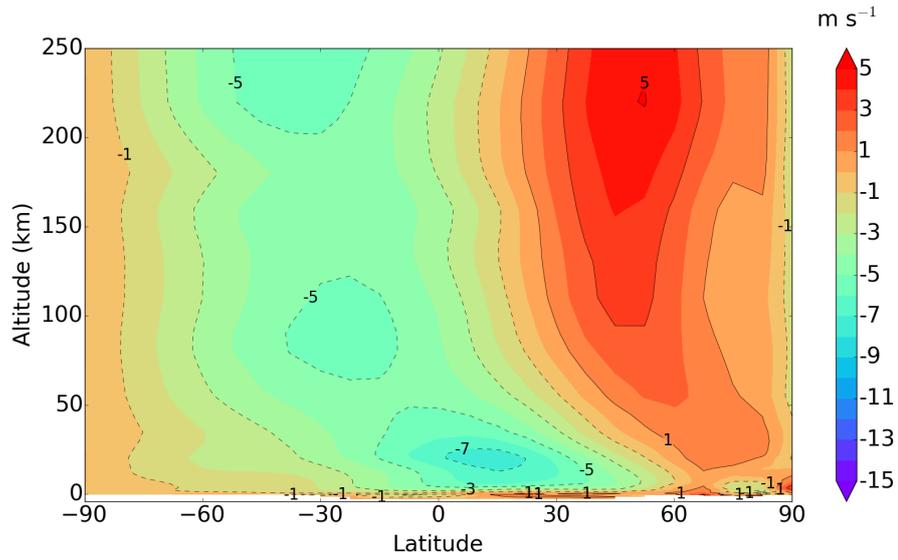


**Figure 11.** Zonal mean zonal winds obtained at  $L_s = 300^\circ$ , obtained from the third year of the low resolution GCM simulation, and showing a  $5 \text{ m s}^{-1}$  prograde jet in the northern hemisphere.

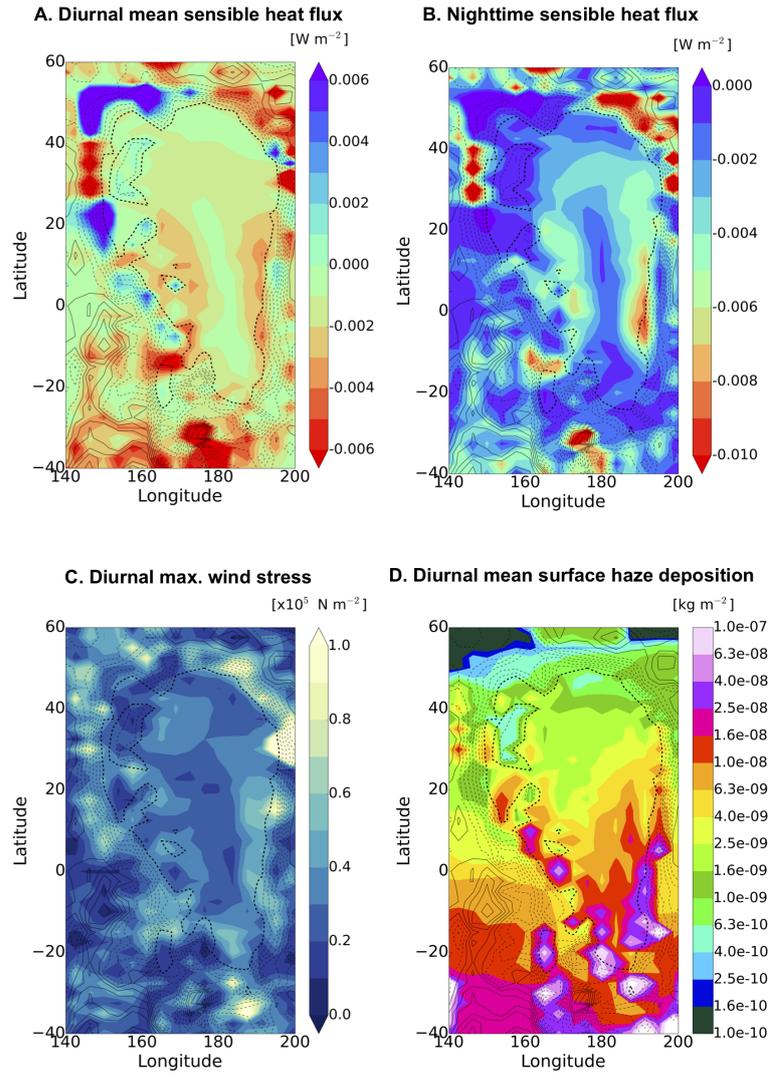


**Figure 12.** GCM results for 2015: different mechanisms in Sputnik Planitia could explain the contrasts in color and composition observed between the western and central regions of the ice sheet. Topography is contoured (contour interval is 300 m). (A) Diurnal mean sensible heat flux ( $\text{W m}^{-2}$ ), negative values indicate downward flux, limiting the nighttime condensation on  $\text{N}_2$  ice. (B) Sensible heat flux averaged during nighttime between 10pm-2am. Sensible heat exchanges are more than one order of magnitude larger over the dark plains than over the bright plains of Sputnik Planitia. (C) Maximal diurnal wind stress on Pluto ( $\text{N m}^{-2}$ ). Higher wind stress values are obtained over the dark plains of Sputnik Planitia. (D) Net surface haze accumulation obtained for one Pluto day in

July 2015 ( $\text{kg m}^{-2}$ ).

D R A F T

October 6, 2019, 10:21pm

D R A F T

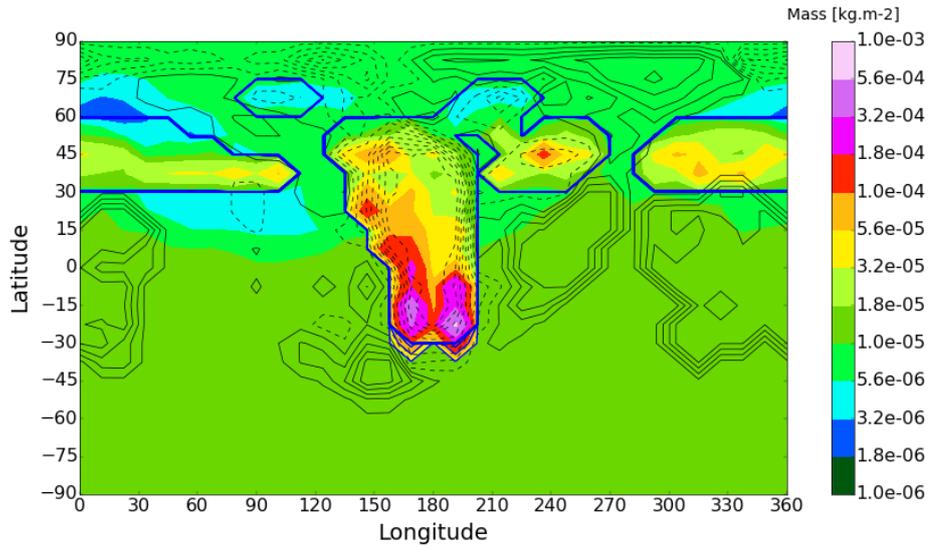


**Figure 13.** Map of surface haze accumulation ( $\text{kg m}^{-2}$ ) obtained with the low-resolution GCM simulation (scenario #2) over the period 1984-2015, assuming 10 nm particles. The blue contours indicate the locations of  $\text{N}_2$  ice deposits. The same simulation performed with  $100 \mu\text{m}$  particles (not shown) shows much less contrast of haze accumulation with longitude, because the sedimentation velocity dominates over the winds, which are less efficient at transporting particles around.

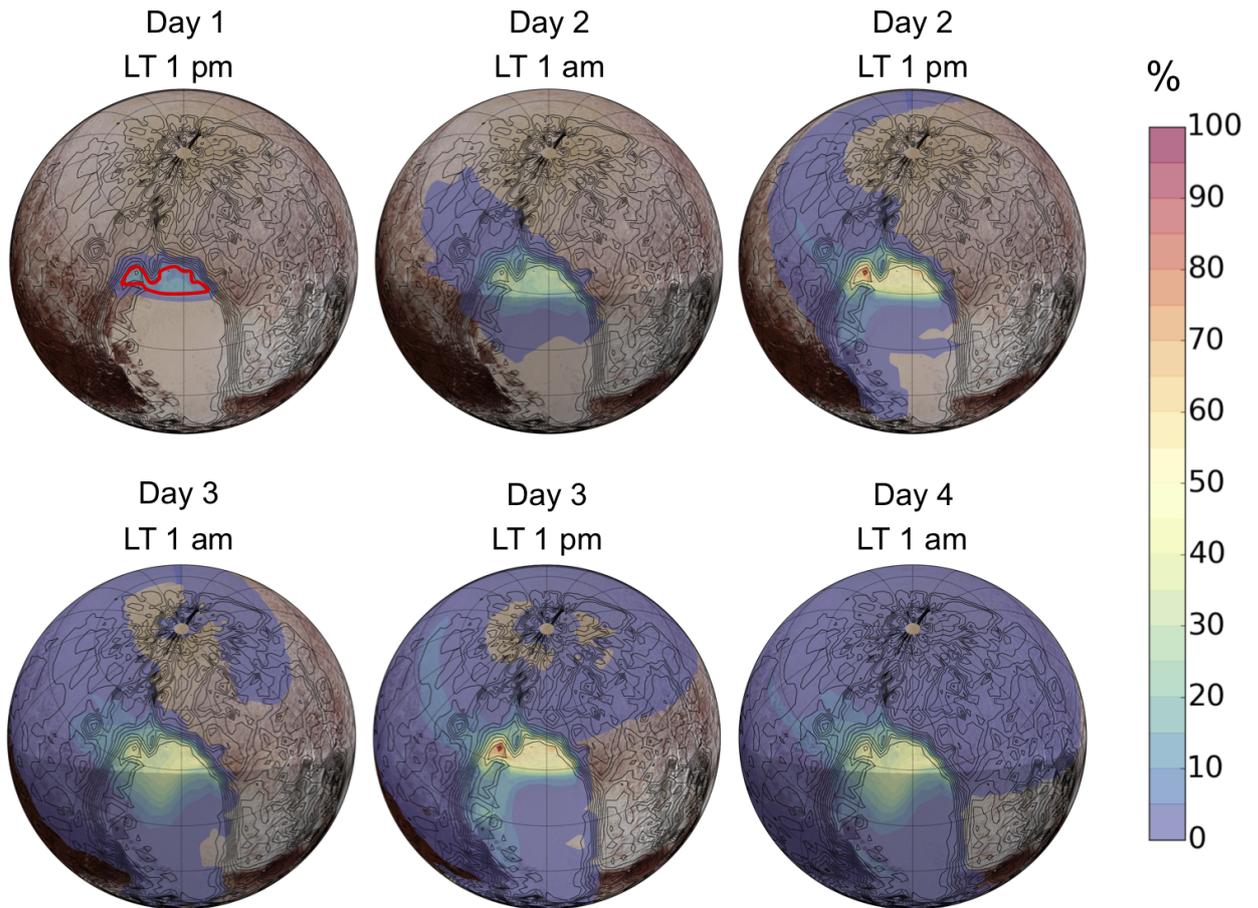


**Figure 14.** Maps of the atmospheric abundance of dark materials obtained with the GCM during three days following the first injection (snapshots at local times 1 pm and 1 am above Sputnik Planitia). The source of dark materials is indicated by the red line on the first panel. The shading indicates nighttime. The colorbar indicates the fraction of dark materials in the atmosphere to the maximal value obtained over the three days (the value depends on the intensity of the source which is not well constrained).

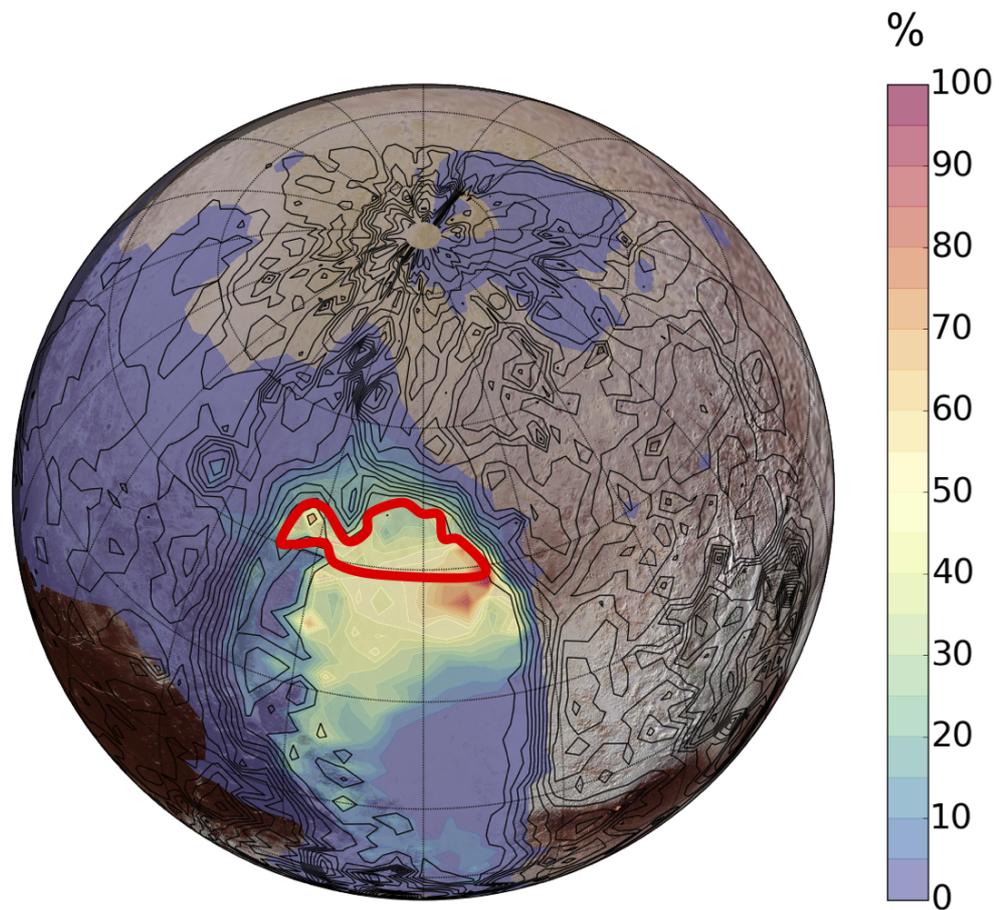


**Figure 15.** Map of the net surface accumulation of dark materials obtained with the GCM after three days following the first injection (snapshots at local times 1 pm above Sputnik Planitia). A larger amount of dark materials is found in the northern and western regions of Sputnik Planitia. The colorbar indicates the fraction of dark materials in the atmosphere to the maximal value obtained.

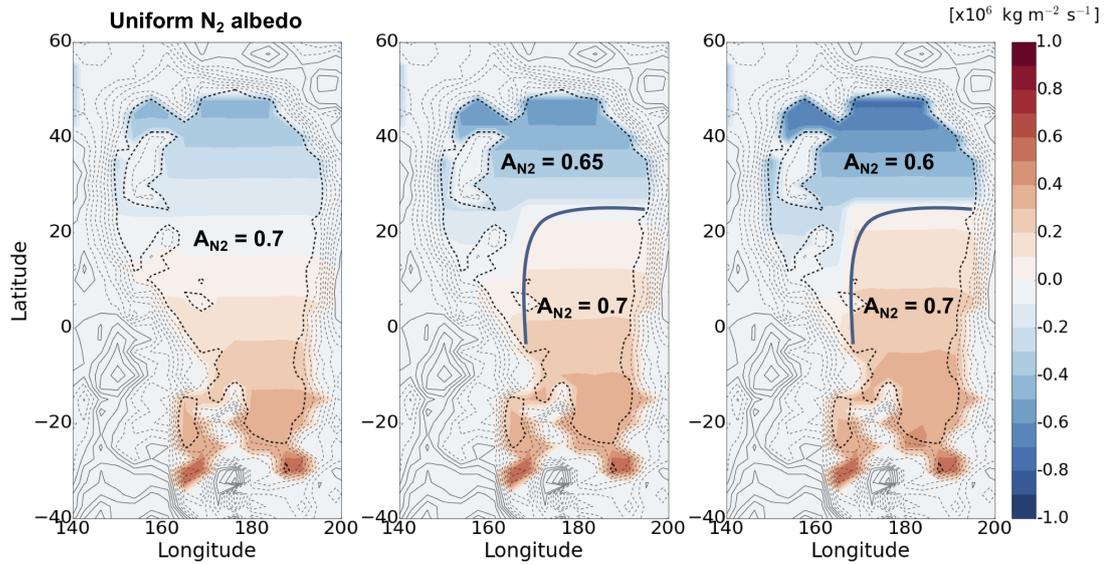


**Figure 16.** Map of the net diurnal budget of N<sub>2</sub> ice in Sputnik Planitia obtained with the GCM for July 2015, for the reference case using a uniform N<sub>2</sub> ice albedo (left), and for cases using a lower albedo in the northern and western regions (center and right).